Machine learning inference of continuous single-cell state transitions during myoblast differentiation and fusion

Amit Shakarchy[1*], Giulia Zarfati[2*], Adi Hazak[2], Reut Mealem[1], Karina Huk[2], Ori Avinoam[2&], Assaf Zaritsky[1&]

[1]Department of Software and Information Systems Engineering, Ben-Gurion University of the Negev, Beer-Sheva 84105, Israel

[2]Department of Biomolecular Sciences, Weizmann Institute of Science, Rehovot 761001, Israel

*Equal contribution

&Co-corresponding authorship

Assaf Zaritsky, assafzar@gmail.com

Ori Avinoam, ori.avinoam@weizmann.ac.il

Abstract

Cells dynamically change their internal organization via continuous cell state transitions to mediate a plethora of physiological processes. Understanding such continuous processes is severely limited due to a lack of tools to measure the holistic physiological state of single cells undergoing a transition. We combined live-cell imaging and machine learning to quantitatively monitor skeletal muscle precursor cell (myoblast) differentiation during multinucleated muscle fiber formation. Our machine learning model predicted the continuous differentiation state of single primary murine myoblasts over time and revealed that inhibiting ERK1/2 leads to a gradual transition from an undifferentiated to a terminally differentiated state 7.5-14.5 hours post inhibition. Myoblast fusion occurred ~3 hours after predicted terminal differentiation. Moreover, we showed that our model could predict that cells have reached terminal differentiation under conditions where fusion was stalled, demonstrating potential applications in screening. This method can be adapted to other biological processes to reveal connections between the dynamic single-cell state and virtually any other functional readout.

Introduction

Single-cell transitions via dynamic changes in protein expression, intracellular organization, morphology, and function, drive many important biological processes, such as progression through the phases of the cell cycle, cellular differentiation, the transition from an immotile to a motile state, or from a living to an apoptotic state. Aberrant cell state transitions lead to various diseases, including cancer and neuromuscular disorders. As such, single-cell state transitions play an inherent role in physiological processes such as embryonic development, tissue regeneration and repair, and in various pathologies.

Obtaining a holistic mechanistic understanding of these processes relies on the ability to continuously measure the physiological state of a cell through time. However, technical limitations, such as the number of live fluorescent state transition reporters that can be simultaneously imaged, hinder the elucidation of cell state transitions as continuous processes. Moreover, state markers that could provide a continuous description are unknown for many biological processes. Consequently, we are currently limited to studying discrete cell states with missing intermediate states, which are often critical (Stumpf et al., 2017; Szkalisity et al., 2021).

Attempts to quantitatively follow cell state dynamics have focused on computational construction of "pseudo-time" trajectories from the integration of fixed cell images (Eulenberg et al., 2017; Gut et al., 2015; Rappez et al., 2020; Stallaert et al., 2022; Szkalisity et al., 2021; Yang et al., 2020). However, the capacity to identify single cell trajectories that deviate from the most common progression, is limited in this approach, due to heterogeneity (Schroeder, 2011). Live cell imaging offers a solution to this challenge by enabling dynamic monitoring and extraction of temporal information at the single-cell resolution. However, unsupervised approaches applied to live cell imaging may still be confounded by variability factors that are unrelated to the state transition of interest (Copperman et al., 2021; Wang et al., 2022).

Here, we combined live cell imaging and supervised machine learning to measure the differentiation state of single cells during skeletal muscle precursor cell differentiation and fusion to form multinucleated muscle fibers ex vivo. The formation of multinucleated muscle fibers is essential for vertebrate muscle development and regeneration. Following injury or growth stimuli, quiescent muscle progenitors called satellite cells become activated to augment the muscle.

Activated satellite cells, often called myoblasts, express myogenic regulatory factors such as MyoD and proliferate to generate the myogenic progenitors needed for muscle regeneration (Bischoff, 1986; Hurme & Kalimo, 1992; Schmidt et al., 2019). After proliferating, myoblasts upregulate the expression of factors such as Myogenin (MyoG) to exit the cell cycle and initiate terminal differentiation, which is accompanied by the downregulation of MyoD (Hernández-Hernández et al., 2017; Lepper et al., 2011; Singh & Dilworth, 2013). Myoblasts initially differentiate into elongated fusion-competent myocytes that migrate, adhere, and fuse with the regenerating muscle fibers (Abmayr & Pavlath, 2012). Newly formed myofibers are characterized by the expression of myosin heavy chain (MyHC; (Bentzinger et al., 2012; Lepper et al., 2011; Yin et al., 2013)). Although significant progress has been made in understanding muscle development, myoblast differentiation, and fusion remain incompletely understood at the molecular and cellular levels owing to several technical challenges. First, myoblasts differentiation and fusion are complex heterogeneous events, confounding systematic investigation. Second, proliferating and terminally-differentiated cells are relatively easy to distinguish morphologically, but there are no markers for intermediate stages of differentiation or means for correlating between differentiation state and specific functions such as motility, morphology, signaling, and fusion.

Here, we trained a machine learning model for measuring the differentiation state of single primary myoblasts ex vivo. Differentiation was induced by pharmacological inhibition of the extracellular signal-regulated kinases (ERK1/2) and experimentally validated by immunofluorescence staining of the differentiation markers MyoD and MyoG (Eigler et al., 2021). Our model predicted that the transition from undifferentiated myoblasts to differentiated myocytes occurs gradually 7.5-14.5 hours after the induction of differentiation. The predicted single-cell differentiation state correlated with the time of fusion, suggesting that differentiation and fusion are temporally coordinated. Pharmacological perturbation of fusion uncoupled differentiation and fusion, leading to the accumulation of differentiated unfused myocytes, which our predictive model computationally validated. These results highlight the potential application of machine learning for continuous cell state inference.

Results

Reduced migration and increased actin expression correlate with myoblast differentiation

We previously established that ERK1/2 inhibition induced robust and synchronous differentiation and fusion of primary myoblasts isolated from chick and mice, leading to the rapid formation of myotubes ex vitro within 24 hours post-induction (Eigler et al., 2021). In order to characterize the dynamic behavior of differentiating myoblasts during the process of myofiber formation, we isolated primary myoblasts from mice endogenously expressing the nuclear marker tdTomato fused to a nuclear localization signal (tDTomato-NLS; (Prigge et al., 2013)) and the live F-actin marker LifeAct-EGFP (Riedl et al., 2008) and performed long-term (23h) time-lapse imaging of large fields of view each containing approximately 3000 cells (Video S1). Live imaging started 1.5 hours after treatment with the ERK1/2 inhibitor SCH772984 (ERKi, 1 μM) (Morris et al., 2013) or with DMSO (control). We observed that differentiation was accompanied by a decrease in cell speed and an increase in LifeAct signal intensity corresponding to an increase in actin expression (Fig. 1A-B, Video S1). These observations are consistent with previous studies linking single-cell migration to lineage choice in differentiating primary hematopoietic progenitors (Buggenthin et al., 2017) and upregulated actin expression with differentiation (Bains et al., 1984; Fischer et al., 2016). To quantify these observations, we automatically tracked all nuclei and extracted from these trajectories the nuclei speed and the actin fluorescence intensity in the field of view as a proxy for the cell migration and actin expression, respectively (Methods). Our quantification validated that cell speed gradually decreased, and actin intensity gradually increased, in concurrence with the advancement in cell differentiation (Fig. 1C-D).

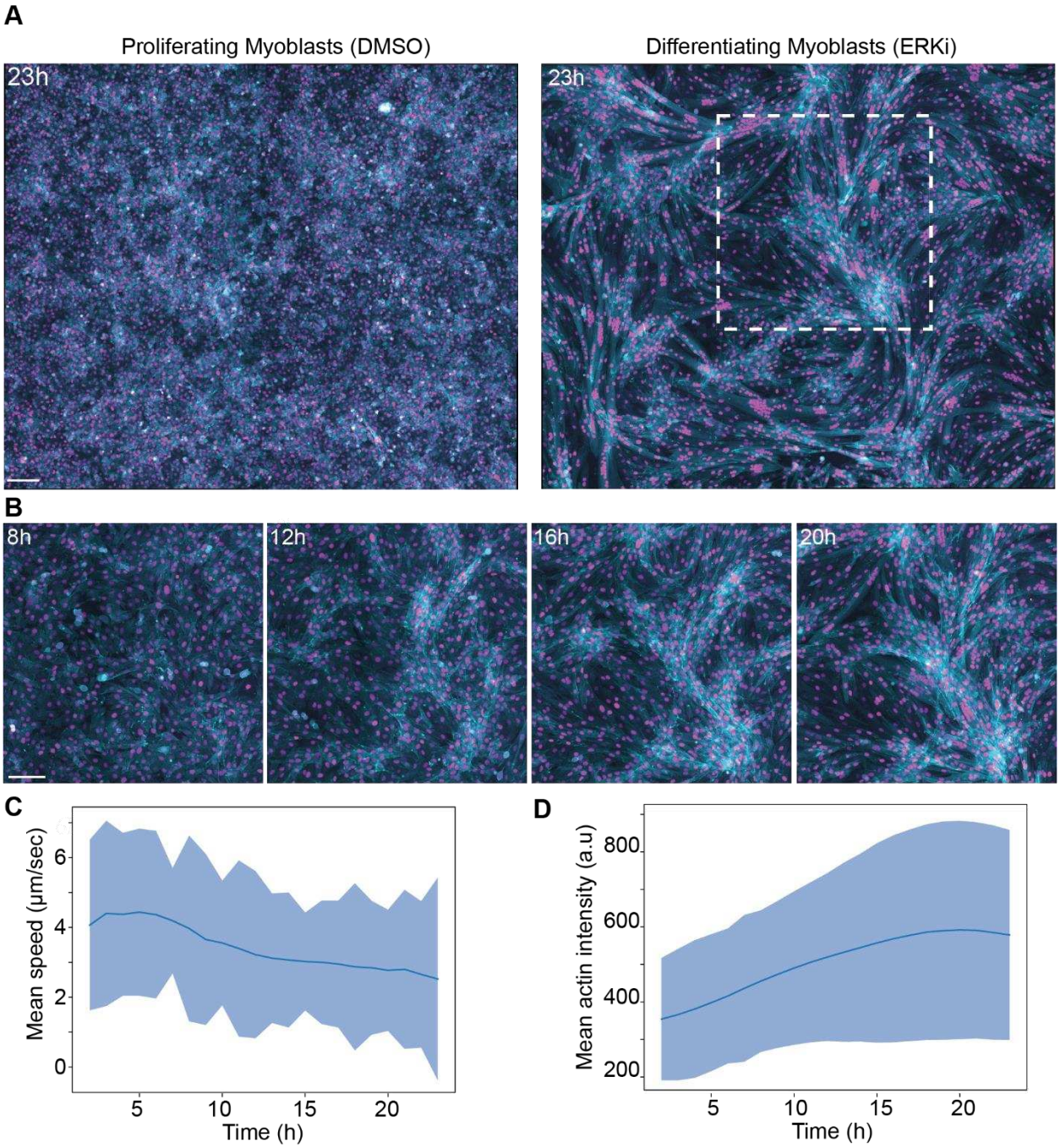

Figure 1. ERKi-treated myoblasts reduce migration speed and increase actin expression during differentiation and fusion

(A) Overlay images of primary myoblasts expressing the nuclear marker tDTomatto-NLS (magenta) and the actin marker LifeAct-EGFP (cyan) 23h after DMSO (control) or ERKi treatment. Square marks the region magnified in B. Magnification 10x. Scale bars 100 µm. (Video S1). **(B)** Magnification (1.5 times) of the region marked at 8, 12, 16, and 20 hours after ERKi treatment. Scale bars 100 µm.
(C) Mean (line) and standard deviation (shade) of single cell speed over time during differentiation (ERKi; ~3000 cells). **(D)** Mean (line) and standard deviation (shade) of actin intensity over time of an entire field of view of differentiating cells (ERKi; Methods).

Measuring continuous single-cell differentiation trajectories with live imaging and machine learning

We hypothesized that the information encoded in single-cell migration trajectories and actin dynamics could be used to determine a continuous score reflecting a myoblast's transition from an undifferentiated to a differentiated state. To achieve this goal, we took a machine learning approach: (1) extracting features from the motility/actin time-series, (2) training machine learning classification models (aka *classifiers*) to discriminate between the undifferentiated and differentiated states, and (3) using the confidence of these models as a quantitative measurement for cell state.

The first step in designing our machine learning model was determining which cells and timeframe can be considered as undifferentiated or differentiated to be used to train our machine learning models. Cells grown in proliferation medium in the presence of DMSO continue to proliferate and remain undifferentiated throughout the experiment, with only a small fraction that begins to differentiate stochastically towards the end of the experiment due to the increase in cell confluence (Eigler et al., 2021). Myocytes fully differentiate before fusion (Abmayr & Pavlath, 2012). Hence, we defined cells as differentiated for classification 2.5 hours before the first fusion event was observed in the field of view (Methods). To enable continuous scoring along single cells differentiation trajectories, we performed semi-manual single-cell tracking, where each trajectory was manually verified and corrected if necessary (Methods) (Video S2). We partitioned trajectories of undifferentiated and differentiated myoblasts to overlapping temporal segments of 2.5 hours each, for an overall 16,636 undifferentiated and 47,819 differentiated temporal segments, extracted from 310 and 538 cells correspondingly, that were used for model training (Fig. 2A - top). From each temporal segment, we extracted the corresponding single cell motility (dx/dt, dy/dt) and actin intensity time series (Methods). Single-cell motility/actin time series features were extracted using the Python package "Time Series FeatuRe Extraction on basis of Scalable Hypothesis tests" (tsfresh) (Christ et al., 2018) that derives properties such as temporal peaks, descriptive statistics (e.g., mean, standard deviation) and autocorrelations (Methods). The extracted single-cell feature vectors and their corresponding undifferentiated/differentiated labels were used to train random forest classifiers (Breiman, 2001), which surpassed other machine learning algorithms (Fig. S1). The entire process is depicted in Fig. 2A and detailed in the Methods.

We applied the trained motility and actin classifiers on single-cell trajectories from an experiment that was not used for training and attained a continuous quantification following the differentiation process by using overlapping temporal segments (Methods). At the population level, the single cell state classification performance gradually increased from an area under the receiver operating characteristic (ROC) curve (AUC) of ~0.6 to ~0.85 at 7.5-14.5 hours from experimental onset (Fig. 2B-C). These AUC values were well beyond the random value of 0.5, indicating that our classifiers can discriminate between undifferentiated and differentiated cells at the population level before appreciable cell morphological changes occur.

Can we use these classifiers to predict the differentiation state of a single cell? For a given temporal segment of a given cell, the classifier outputs a "confidence score" (i.e., differentiation score) that reflects the model's certainty in its prediction. Low differentiation scores indicate that the cells are predicted as undifferentiated, while high scores indicate predicted differentiation. To interpret what temporal features were the most important for the models' prediction, we applied SHapley Additive exPlanations (SHAP) (Lundberg & Lee, 2017) and used random forest's feature importance algorithms (Breiman, 2001). Both interpretability methods highlighted temporal features related to high variance of acceleration rate or high complexity of actin intensity time series as dominant features driving the models' prediction (Fig. S3). We hypothesized that the differentiation score could be used as a continuous readout for the cell state. At the critical time frame of 7.5-14.5 hours, at the population level, the differentiation scores of ERKi-treated cells gradually increased for both the motility (Fig. 2D) and the actin-based models (Fig. 2E), while maintaining low scores for experiments of DMSO-treated cells. We conducted a single-cell analysis by measuring the Spearman correlation between single-cell differentiation score and time at the critical time interval of 7.5-14.5 hours when differentiation occurs. This analysis indicated that most cells underwent a monotonic increase in differentiation scores over time (Fig. 2F). A similar gradual increase in differentiation score at 7.5-14.5 was observed when flipping the experiments used for training and testing (Fig. S4), the differentiation score was not sensitive to the size of the temporal segment (Fig. S5), and to the window size used for actin measurements (Fig. S6). If the models' scores reflect a quantitative measurement for the cells' differentiation state, the gradual increase at the population level can result from a synchronized gradual transition of single cells from undifferentiated-to-differentiated states at similar times or of an

unsynchronized abrupt transition of single cells at different time points. Visualizing single-cell trajectories showed that most trajectories followed a gradual increase in their differentiation scores, but abrupt transitions were not observed (Fig. 2G). We quantified this by measuring the predicted duration of the differentiation process (Methods), suggesting that the main progression in single-cell differentiation is highly heterogeneous (Fig. 2H), with a general agreement between the motility- and actin-based classifiers' predictions (Fig. S7). These results supported the former mechanisms of synchronized and gradual-continuous transition from an undifferentiated to a differentiated state within a typical timeframe.

To experimentally validate our prediction of gradual differentiation at the critical time frame, we fixed the cells at different time points (0h - 6h -8h -10h - 12h -14h – 16h – 24h) and performed immunofluorescence staining of the differentiation markers MyoD, MyoG and MyHC (Methods). Primary myoblasts initially express MyoD. Differentiation into fusion-competent myocytes is accompanied by the upregulation of MyoG and downregulation of MyoD, which initiates terminal differentiation. MyHC is exclusively expressed after terminal differentiation, predominantly in myofibers. As expected and consistent with the classification results, we observed that the number of MyoG-expressing cells increased over time, stabilizing at 14 hours post-induction, while the number of MyoD-expressing cells decreased (Fig. 2I). MyHC expression began at 16h post-induction, and was predominantly in the multinucleated myotubes at 24hr, indicating that the cells have differentiated and fused (Fig. S8, Fig. S9). Altogether, our data suggest that machine learning can transform motility and actin dynamics to a quantitative readout characterizing the myoblast differentiation process at single-cell resolution describing a continuous myoblast state transition from an undifferentiated to the terminally differentiated states at 7.5-14.5 hours post ERKi.

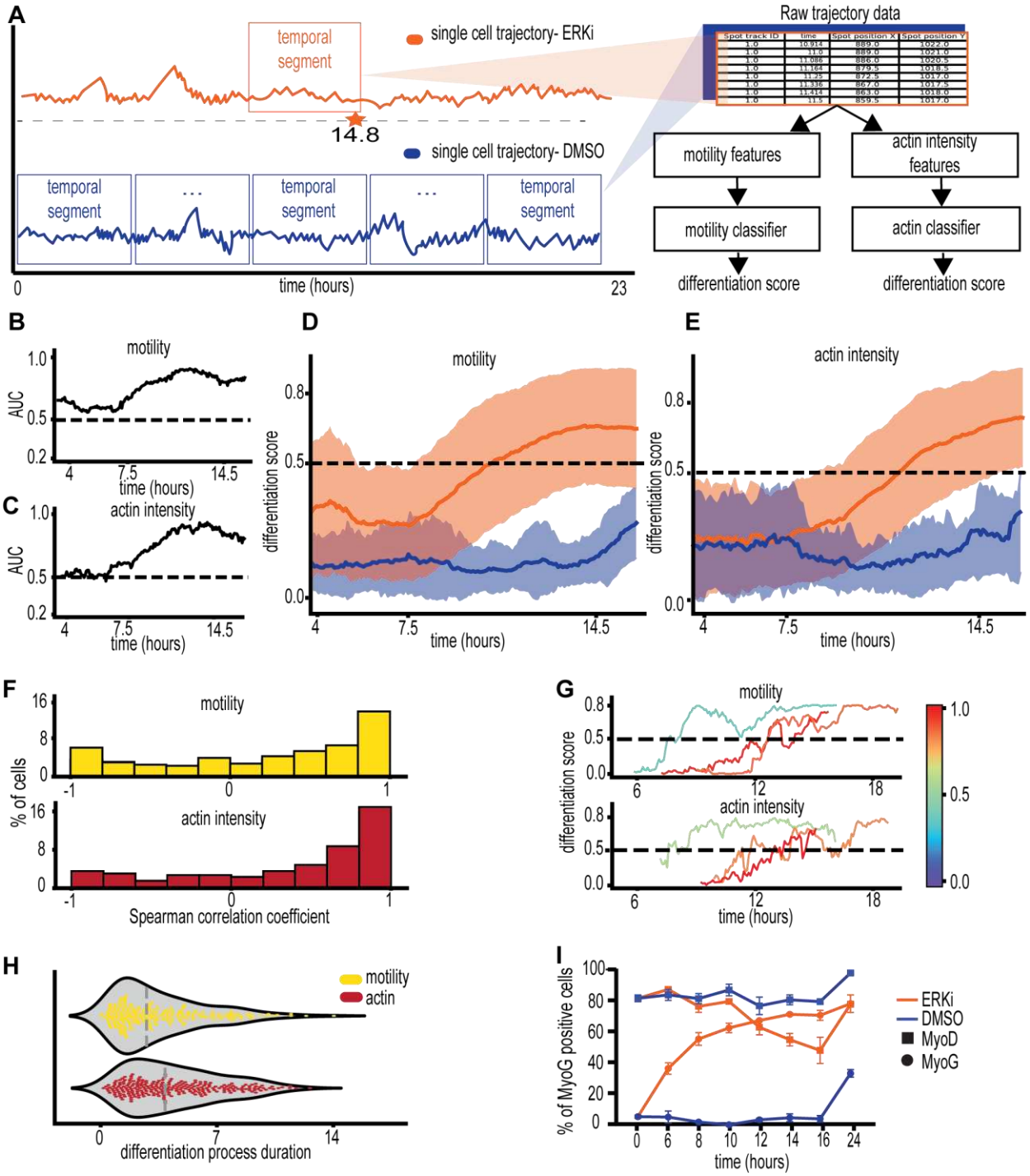

Figure 2. Inference of single cells differentiation trajectories by machine learning applied to actin/motility dynamics

(A) Training Random Forest classifiers to predict single cells' differentiation state - cartoon. Left: single cell motility/actin time series are partitioned into temporal segments of 2.5 hours each. Positive labels were assigned to the ERKi-treated cells' segment (top, orange) starting 2.5 hours before the first fusion event (orange star on the dashed timeline). Negative labels were assigned to all segments of DMSO-treated cells (blue). Right: features extracted from the positive (orange) and negative (blue) time series

(top) were used to train classification models. Two models, one based on motility and the other on actin intensity, were trained based on time series extracted from the single-cell trajectories. **(B-C)** Classification performance. Area under the receiver operating characteristic (ROC) curve (AUC) over time for classifiers trained with motility (B) and actin intensity (C) time-series. The AUC was calculated for 789 cells from an independent experiment. Classification performance of a random model (AUC = 0.5) is marked with a dashed horizontal line. **(D-E)** Mean (solid line) and standard deviation (shade) of the differentiation score over time of ERKi (orange) and DMSO (blue) treated cells using the motility (B) and the actin intensity (C) classifiers. The analysis for the entire experiment is shown at (Fig. S2). **(F)** Distribution of single-cell Spearman correlation between the classifier's score and time, calculated for motility (orange) and actin (red) classifiers. **(G)** Representative single cells differentiation trajectories inferred by the motility (top) and the actin (bottom) classifiers. Trajectories are colored according to the Spearman correlation between their corresponding differentiation score and time. **(H)** Distribution of the single cell predicted duration of the differentiation process, as measured by the motility (yellow) and actin intensity (red) classifiers' prediction: the time passed between a stable low threshold of 0.2-0.3 and a high stable threshold of 0.7-0.8 (full details in Methods). The median predicted duration of the differentiation process was 3.3 (motility) and 4.5 (actin intensity) hours. **(I)** Percentage of MyoG and MyoD positive cells over time. Proliferating myoblasts, DMSO-treated cells (blue), differentiating myoblasts, ERKi-treated cells (orange). MyoD (square) and MyoG (circle), bars show the StDv between 3 experimental replicates.

Effective discrimination is not sufficient for the quantitative characterization of continuous state transitions

Using the simplest readouts to quantify and discriminate different biological conditions/states is always preferred because it provides more direct insight regarding the underlying mechanisms. Is it possible that our approach is overly complicated and exceeds what is required to quantitatively describe the differentiation process? Are straight-forward single-cell measurements sufficient to discriminate between undifferentiated and differentiated cells and follow the differentiation process? To test this possibility, we evaluated the discriminative performance of single-cell properties that are expected to deviate between the DMSO and ERKi-treated cells. These included cell speed, actin intensity, migration persistence, and local density. The local density dramatically increased over time for DMSO-treated cells due to continued proliferation throughout the experiment (Fig. 3A). The mean speed and actin intensity of DMSO-treated cells slightly decreased and increased correspondingly over time, perhaps due to the increased density (Fig. 3B-C). Persistent migration of DMSO-treated cells was lower compared to ERKi-treated cells without a clear trend over time (Fig. 3D). Each of these four discriminative readouts, as well as their integration, could be generalized across experiments as demonstrated by using each feature to train

a machine learning model and applying this model to discriminate between the two experimental conditions in an independent experiment (Fig. 3E, Methods).

The model trained with the local density and the model trained with all four features surpassed the discrimination performance of the time-series motility and actin models (also reported in Fig. 2B-C). However, discrimination does not necessarily imply that these readouts can be used to quantitatively describe the differentiation process. Indeed, the differentiation score of each of these classifiers could not capture the differentiation process as measured by single-cell monotonic increase at the critical differentiation time interval of 7.5-14.5 hours. The single cell correlations between the differentiation score and time were distributed around zero for all the single-feature classifiers, as well as for the integrated classifier (Fig. 3F). This is in contrast to our classifiers that generalized to effectively quantify the differentiation process leading to a higher correlation between the differentiation score and time (Fig. 3F - motility, actin intensity, same data as in Fig. 2G). A plausible explanation for why these effective discriminating models could not capture the continuous differentiation process is that the discriminating features captured properties attributed to the undifferentiated state. For example, the increased local cell density of DMSO-treated cells can be used to discriminate effectively but does not provide any information regarding the progression through differentiation. Indeed, training models that included temporal features extracted from single-cell local density dynamics showed the same or deteriorated correlation between the differentiation score and time compared to models that were not trained with local density (Fig. S10). These results indicate that effective discrimination between the discrete extreme states is insufficient for the quantitative characterization of continuous state transitions. Specifically, using machine learning for quantitative characterization requires extracting features that can capture the state transition and avoiding features that may confound the quantitative characterization of the process (e.g., avoiding local cell density in characterizing the differentiation process).

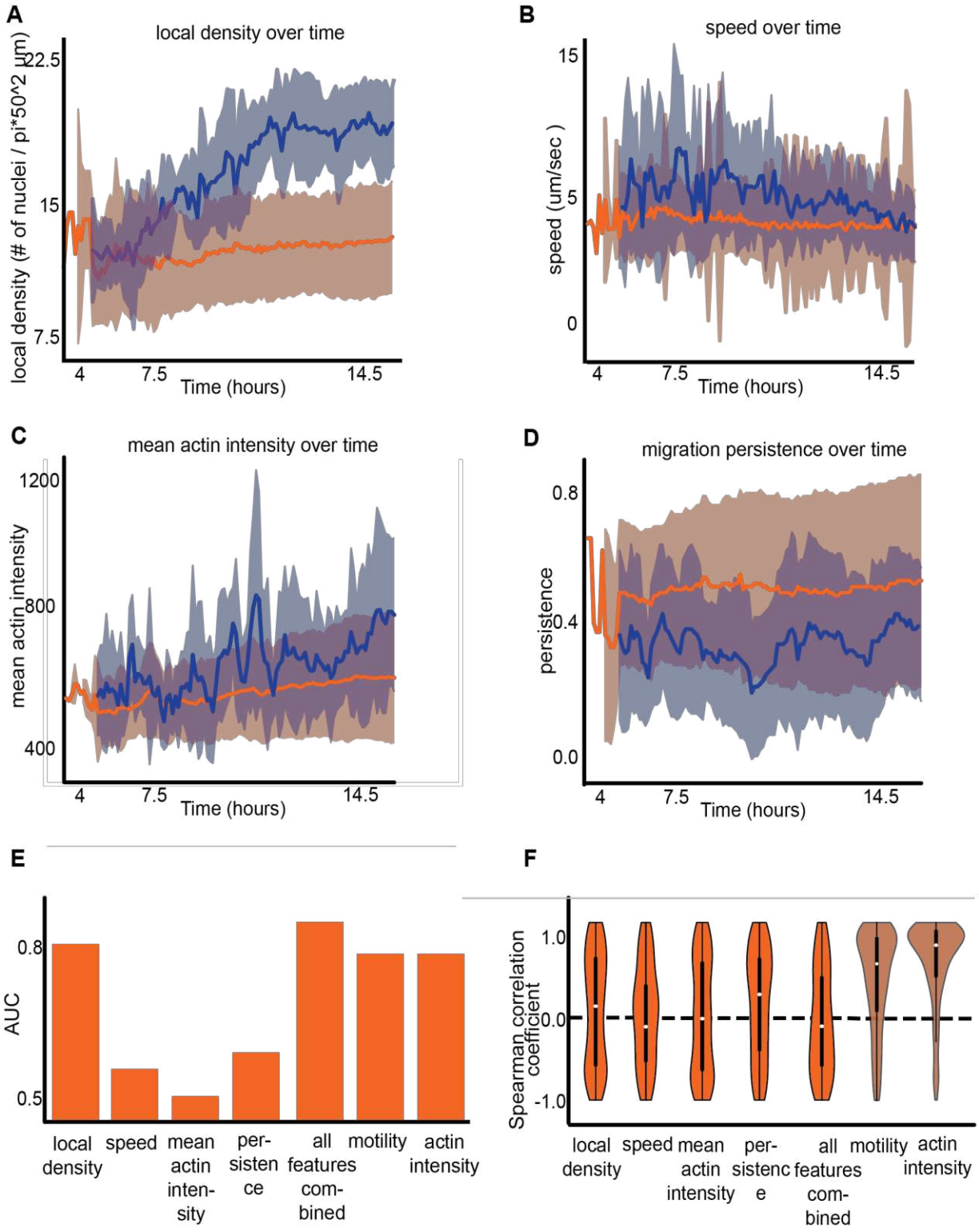

Figure 3. Simple single-cell measurements are insufficient for continuous cell state transition characterization

(A-D) Mean (solid line) and standard deviation (shade) of single cell characteristics over time of ERKi- (orange) and DMSO- (blue) treated cells. Single-cell properties included are local cell density (A), mean speed (B), mean actin intensity (C), and persistence in migration (D). **(E)** Single-cell state classification performance. Area under the receiver operating characteristic (ROC) curve (AUC) for classifiers trained using speed, mean actin intensity, persistent migration, local cell density, and integration of these properties to discriminate ERKi- and DMSO-treated cells experimental conditions. The right-most bars show AUCs for classifiers trained with motility and actin dynamics. AUC scores were calculated for 757 temporal segments of differentiated/undifferentiated cells from an experiment that was not used for model training (full details in Methods). **(F)** The single-cell correlation distribution between the differentiation score and time for all the classifiers shown in panel E (median shown in white). Dashed horizontal line shows no correlation. The right-most distributions show correlations for classifiers trained with motility and actin dynamics.

Myoblast differentiation and fusion are temporally coupled

We next aimed at harnessing our ability to infer continuous differentiation scores of single myoblasts to investigate the relations between cell differentiation and fusion. We manually annotated the fusion time of 68 myoblasts that fused to 6 myofibers (Fig. 4A, Methods) and used the continuous differentiation score to determine an estimated time of terminal differentiation state (Methods). Both the distributions of the single cells' terminal differentiation and fusion times followed a normal-like distribution, where the variability in the predicted differentiation time was higher than that of fusion time (Fig. 4B). The time duration between terminal differentiation and fusion also followed a normal-like distribution, indicating a typical duration of ~3 hours between terminal differentiation and fusion at the population scale (Fig. 4C). These results suggest that cells undergo fusion within a typical time interval from their terminal differentiation. This coupling was validated by measuring a correlation between single-cell differentiation and fusion times (Fig. 4D) and was not sensitive to the threshold used to determine the terminal differentiation time (Fig. S12).

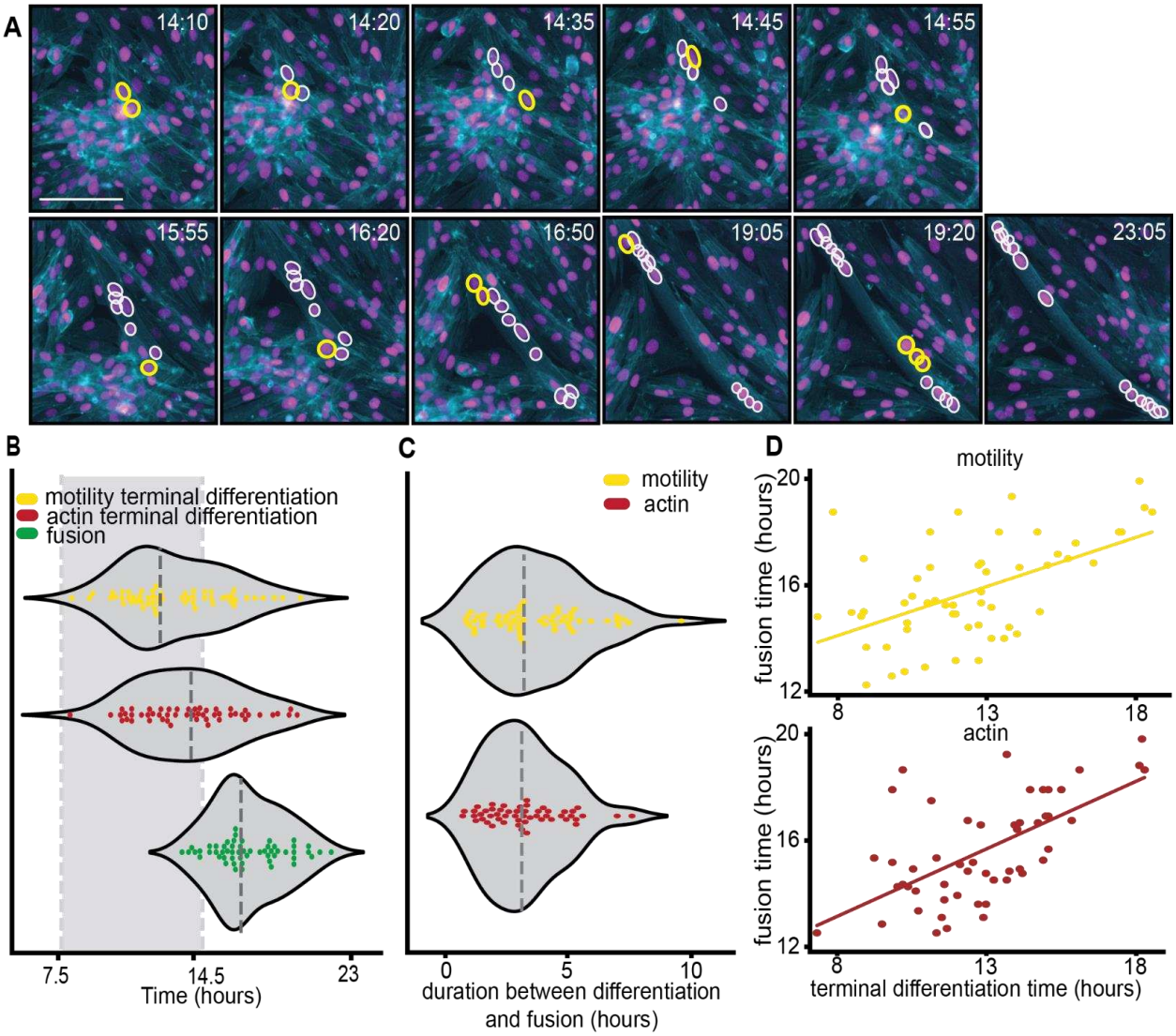

Figure 4. Correlation between terminal differentiation and fusion time

(A) Annotations of single-cell fusion into a representative myofiber over time. Cells marked in white are already fused, and cells marked in yellow are fusing into the fiber. Scale bar 100 µm. **(B)** Distribution of single cells' fusion times (green) and terminal differentiation times determined by motility (yellow) and actin intensity (red) classifiers. The dashed vertical gray rectangle highlights the differentiation time interval of 7.5-14.5 hours. All three distributions were normal-like as assessed by the D'Agostino's K-squared test not rejecting the null hypothesis that the terminal differentiation time was normally distributed (motility classifier: p-value = 0.36, actin classifier p-value = 0.64; fusion time p-value = 0.1). The "terminal differentiation" state was determined using a differentiation score threshold of 0.78 (the same threshold was also used in panels C-D). The models identified 56 (motility) and 52 (actin intensity) cells that reached a terminal differentiation state. 71% (motility) and 65% (actin intensity) of the identified cells reached a terminally differentiated state by 15 hours post-induction. The median time of terminal differentiation was 12.63 (motility) and 14.2 (actin intensity); the median fusion time was 16.8 hours. **(C)** Distribution of the duration between single cell terminal differentiation and fusion, for terminal differentiation determined by motility (yellow) and actin (red) classifiers. Both distributions were normal-like as assessed by the D'Agostino's K-squared test not rejecting the null hypothesis that the duration was

normally distributed (motility classifier: p-value = 0.13, actin classifier: p-value = 0.13). Median differentiation-to-fusion duration was 3.1 (motility) and 3 (intensity) hours.
(D) Associating single cell terminal differentiation time (x-axis) and fusion time (y-axis), determined by the motility (yellow) and the actin (red) classifiers. Pearson correlation coefficients were 0.52 (motility) and 0.73 (actin intensity), $p < 0.001$ for both actin and motility classifiers.

Co-inhibition of P38 and ERK1/2 leads to differentiation but not to fusion

The molecular machinery that drives myoblast fusion is not fully elucidated largely because distinguishing between components essential for differentiation from those essential for fusion is challenging. To test whether our approach can be used to distinguish differentiation from fusion, we aimed to experimentally uncouple differentiation and fusion by identifying a condition leading to the accumulation of differentiated but unfused cells.

Previous studies have shown that co-inhibition of p38, a family of MAP kinases that play a critical role in the initiation of the differentiation program, together with a promyogenic factor, overcomes the early block in differentiation but not the later impairment of muscle cell fusion imposed by the p38 inhibitor, leading to differentiated unfused cells (Gardner et al., 2015). Following this logic, we treated primary myoblasts with the promyogenic ERKi and the P38 inhibitor BIRB 796 (P38i; 5 μM) and performed primary myoblasts live imaging experiments. There was little appreciable difference between cells treated with P38i and those treated with DMSO, consistent with previous studies showing that P38i maintains myoblasts in a proliferative undifferentiated state (Zetser et al., 1999). Myoblasts co-treated with ERKi and P38i appeared differentiated with similar motility and actin intensity attributes, but failed to fuse, leading to the complete absence of multinucleated myofibers (Fig. 5A-B). Immunofluorescent staining validated that the fraction of MyoG-positive cells remained low for P38i treated cells and increased in cultures cotreated with P38i and ERKi, indicating that co-inhibition of P38 and ERK1/2 leads to *bona fide* differentiation (Fig. 5C, Video S3). The fraction of MyoD-positive cells remained high for P38i and decreased moderately in cultures cotreated with P38i and ERKi (Fig. 5D). However, it was not clear whether the differentiation process was altered with respect to ERKi-treated cells. Thus, we quantitatively described the differentiation process of cells cotreated with P38i and ERKi by applying our motility and actin models trained with DMSO and ERKi-treated cells data. The differentiation profile of P38i-ERKi-treated cells followed a trend strikingly similar to the one obtained for ERKi-treated cells and specifically included the gradual transition at the critical time of 7.5-14.5 hours

(Fig. 5E-F). As a control, we validated that the profile of P38i-treated cells resembled that of proliferating cells treated with DMSO alone. These results suggest that our model can predict the cell differentiation state regardless of perturbed fusion, which is essential for the future identification of molecules specifically required downstream of differentiation during fusion. Moreover, these results suggest that the differentiation process is not altered upon perturbed fusion and thus provide complementary evidence supporting the notion that differentiation and fusion can be uncoupled using P38 inhibition with a promyogenic signal to overcome the inhibition and initiate differentiation in the absence of P38.

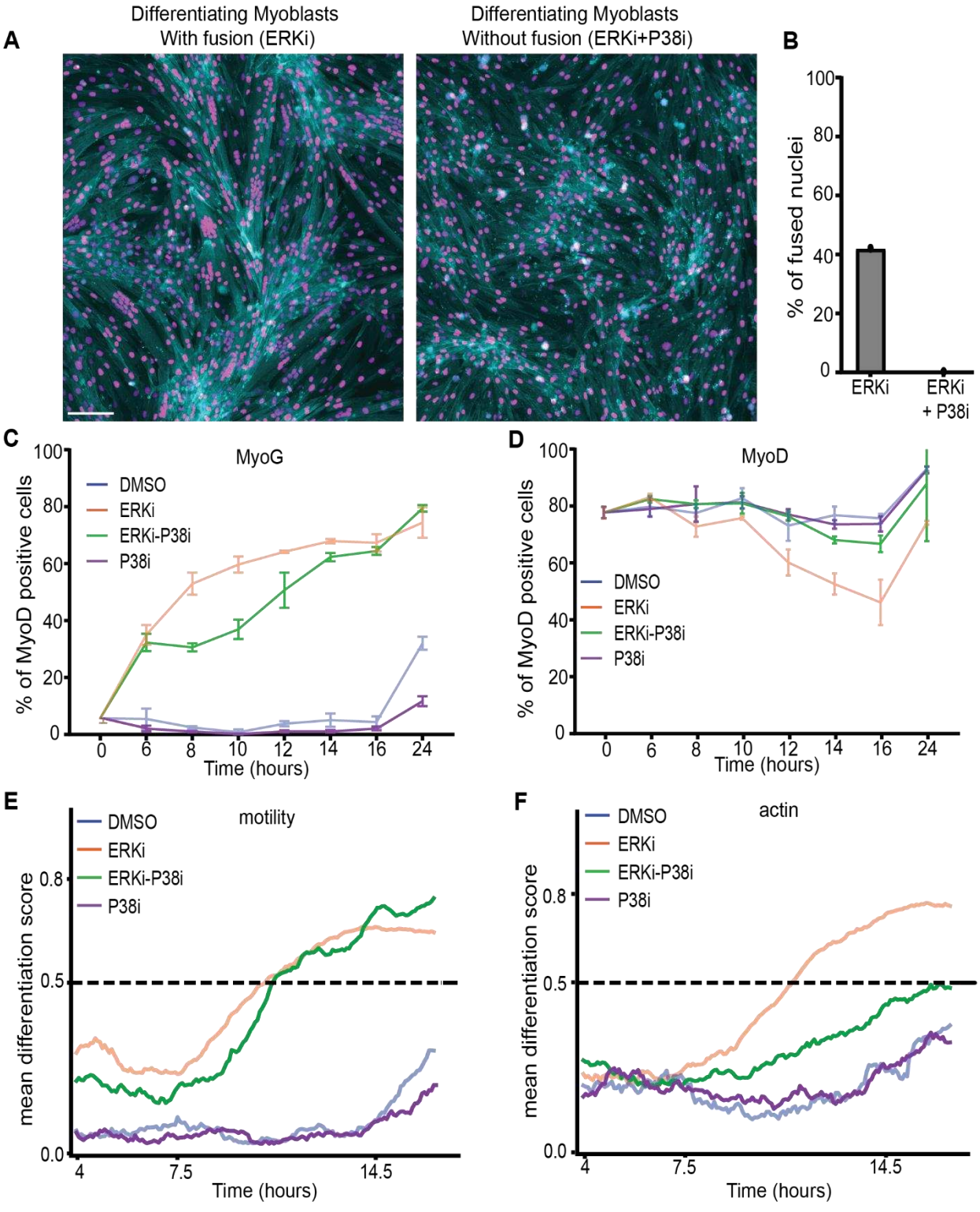

Figure 5. Uncoupling differentiation and fusion with experiments and machine learning validations

(A) Representative images of myoblasts treated with ERKi (left) and myoblasts co-treated with ERKi and P38i (right) at 23 hours. ERKi-treated cells differentiate and fuse, ERKi- and P38i-treated myoblasts

undergo differentiation but do not fuse. Scale bar 100 μm. **(B)** Fusion Index: Percentage of fused nuclei in ERKi and ERKi-P38i treatments. **(C)** Percentage of MyoG positive cells in DMSO (blue), ERKi (orange), ERKi + P38i (green), and P38i (purple) treated cells. MyoG positive cells percentage for ERKi- and DMSO-treated cells are the same as shown in Fig. 2. **(D)** Percentage of MyoD positive cells under proliferation conditions (DMSO; blue), differentiation (ERKi; orange), differentiation without fusion (ERKi + P38i; green), and proliferation (P38i; purple). The MyoD data for ERKi- and DMSO- treated cells are the same as shown in Fig. 2. **(E-F)** Mean differentiation score over time of ERKi- (orange), DMSO- (blue), ERKi+P38i- (green), and P38i- alone (purple) treated cells using the motility (C) and actin intensity (D) classifiers. ERKi- and DMSO- treated cells differentiation scores are the same as in Fig. 2. The analysis for the entire experiment is shown at (Fig. S11).

Discussion

We combined live cell imaging and machine learning to infer the differentiation state of single cells during the process of muscle fiber formation. Many studies highlight the rich information encapsulated in single-cell dynamics that, with the aid of supervised or unsupervised machine learning, enable effective identification of sub-populations and discrimination of perturbations (Choi et al., 2021; Goglia et al., 2020; Jacques et al., 2021; Jena et al., 2022; Kimmel et al., 2018; Valls & Esposito, 2022), that cannot be inferred from static snapshot images (Copperman et al., 2021; Wang et al., 2020). For example, approaches that rely on static snapshots make it extremely hard to infer trajectories that deviate from the mainstream cell state progression because they are confounded by cell-to-cell variability. The ability to measure a single cell state as it transitions through time during a physiological process, along with careful experimental-computational interplay, enabled us to quantitatively follow the process and identify the key time frame where myoblasts gradually undergo differentiation (Fig. 2D-E), link single-cell differentiation to fusion (Fig. 4D), and validate that perturbed fusion with P38 inhibition does not alter the differentiation process (Fig. 5E-F).

The ability to infer the differentiation state of individual myoblasts can further enable the identification of novel myogenic factors, high throughput screening for proregenerative compounds, and the definition and subsequent examination of distinct intermediate steps in the differentiation process. Moreover, this approach of harnessing temporal dynamics by machine learning, without explicit state markers, can be generalized beyond terminal differentiation. Such a computational estimation of the cell state may have wide applications in characterizing other single-cell dynamic functions such as transitioning during the cell cycle, epithelial to mesenchymal transition, immotile to motile, disease progression, and cell death. The dynamic state readout can be correlated to other, independently measured cell readouts to systematically characterize the full spectrum of heterogeneities in complex biological processes.

Unsupervised approaches for cell state inference traverse from an initial to a final state through steps that rely on similarity in cell appearance (Gut et al., 2015). These trajectories can be distorted by batch effects or cell phenotypes unrelated to the state transition. In our approach, the supervised component forces the trajectory to follow the phenotypic axes most relevant to the state transition under investigation. This approach is similar to the approaches taken by (Szkalisity et al., 2021),

which rely on the manual assignment of cells to discrete states in 2D that are then inferred by regression analysis, or by (Stallaert et al., 2022) that uses a supervised model to select features predictive of the cell state before constructing cell state trajectories.

Our approach uses the physiological cell state (undifferentiated vs. differentiated) as the ground truth, optimizes binary classification, and uses the classification's confidence score as the cell state measurement. However, there is no guarantee that the classification's confidence score has linear properties. For example, whether the difference in scores between 0.3 and 0.4 has the same phenotypic magnitude as between scores of 0.6 and 0.7. This limitation is also common to approaches that use non-linear dimensionality reduction (Copperman et al., 2021; Eulenberg et al., 2017; Jacques et al., 2021; Rappez et al., 2020; Stallaert et al., 2022; Wang et al., 2022) and could also limit unsupervised state representations that can be dominated by features that do not relate to the cell state (Copperman et al., 2021; Jacques et al., 2021; Wang et al., 2022). Still, the monotonicity property holds, e.g., a differentiation score of 0.4 is predicted to be more advanced along the differentiation trajectory than a differentiation score of 0.3. This implies that the machine learning model captures more phenotypic evidence for the advancement along the state transition axis. This monotonicity property is sufficient for comparing different trajectories and calculating temporal correlations between cell state and other properties, as demonstrated here and elsewhere (e.g., (Mayr et al., 2021; Zaritsky et al., 2021)).

Methods

Mouse lines

We used Actin and nuclear reporters mice (LifeAct-GFP/ nTnG$^{+/+}$) (Eigler et al., 2021). Fluorescence expression validated using visual inspection. All experiments were approved by the Animal Care and Use Committee of the Weizmann Institute of Science (IACUC application #07690920-3).

Isolation and treatment of primary myoblasts

Primary mouse myoblasts were isolated from gastrocnemius muscle using mechanical-tissue dissociation as in (Eigler et al., 2021). Briefly, after cutting the muscle tissue into small pieces, they were incubated in Trypsin EDTA Solution B (0.25%Tripsin and 0.5% EDTA, Biological Industries Israel) and subjected to mechanical dissociation with a serological pipet. Supernatants were strained (FALCON REF no.352340) and centrifuged. Cell pellets were resuspended in BioAMF^{TM}-2 media (Biological Industries, Israel), plated on 10% Matrigel® Matrix (Corning REF no. 354234) coated plates, and grown at 37° in a 5% CO_2 incubator. Bio-AMF^{TM}-2 was used in all experiments (Biological Industries Israel).

Microscopy

For live imaging, 40.000 cells were plated in a Slide 8-well chamber (Ibidi GmbH, cat.no.80826) coated with 10% Matrigel® Matrix. 15hr after cell seeding, the different treatments were added to the cells cultured in proliferation medium Bio-AMF^{TM}-2 (Biological Industries Israel). To induce myoblasts differentiation, cells were treated with 1µM ERK inhibitor (SCH 772984 CAYMAN CHEMICAL COMPANY). The inhibitors are dissolve in Dimethyl Sulfoxide (DMSO, MP Biomedicals cat.no 196055, 1.10g/ml stock concentration). Therefore, in the control sample of proliferation, DMSO treatment was added in a concentration of 1 µg/ml (equal to 1 µl, the volume added of each inhibitor). In the samples treated with P38 inhibitor, were used 5 µM (BIRB 796, AXON 1358) either alone or together with ERKi.

Live imaging (37°C, with 5% CO2) was performed using Cell discoverer 7-Zaiss inverted in widefield mode with Zeiss Axiocam 506 camera Carl Zeiss Ltd. Images were acquired using a ZEISS Plan-APOCHROMAT 20x / 0.70 Autocorr Objective (Working distance 2.20 mm).

Excitation 470nm for GFP signals (LifeAct) and 567nm for tdTomato (nuclei). ZEN blue software 3.1 was used for image acquisition. If necessary, linear adjustments to brightness and contrast were applied using ImageJ v1.52 software (Schindelin et al., 2012). Cells were imaged 1.5 hours after adding the treatments, with 5 min intervals and at a pixel size of 0.462 µm.

Fixed samples were imaged using a ZEISS Plan-APOCHROMAT 5x / 0.35 Autocorr Objective (Working distance 5.10 mm), 1.178 µm/px. Excitation 470nm for GFP (MyHC) and 567nm for Alexa Fluor® 568 (MyoG - MyoD) and 405nm for nuclei stained with Hoechst 33342.

Immunofluorescence staining of MyoG-MyoD-MyHC

Primary myoblasts were seeded in a 96-well culture dish, coated in Matrigel® Matrix at 8,000 cells per well cultured in BioAMF-2 media. After 15h incubation at 37° in a 5% CO_2 incubator, the cells were treated with 1µM ERK inhibitor (SCH 772984 CAYMAN CHEMICAL COMPANY) and 5 µM P38 inhibitor (BIRB 796, AXON 1358) in the needed samples. The inhibitors are dissolve in Dimethyl Sulfoxide (DMSO, MP Biomedicals cat.no 196055, 1.10g/ml stock concentration). Therefore, in the control sample of proliferation, DMSO treatment was added in a concentration of 1 µg/ml (equal to 1 µl, the volume added of each inhibitor). Cells were fixed at specific time points (0h-6h-8h-10h-12h-16h-24h) with 3.7% PFA in PBS for 15 minutes at room temperature. The cells were then quenched with 40mM ammonium chloride for 5 min, washed with PBS 3 times, permeabilized in PBS with 0.01% Triton x-100 for 10 min, and blocked in 10% FBS in PBS (blocking buffer) for 1h at room temperature. Primary antibody incubation was done in a blocking buffer overnight at 4 degrees, with the following antibodies: Anti-Fast Myosin Heavy Chain antibody [MY-32] (Ab51263), abcam) 1:400, Anti-Myogenin antibody [EPR4789] (ab124800) 1:500, and Anti-MyoD1 antibody (ab64159) 1:50. Cells were washed 3 times in PBS and then incubated with secondary antibodies: Goat Anti-Mouse IgG H&L (Alexa Fluor® 488) (ab150117) 1:600, Donkey Anti-Rabbit IgG H&L (Alexa Fluor® 647) (ab150067) 1:600, Donkey Anti-Rabbit IgG H&L (Alexa Fluor® 568) (ab175692) 1:600. The cells were washed 3 times in PBS, incubated with Hoechst 33342 (Thermo Scientific cat no.62249, 1:1000) for 5 min and washed in PBS.

Quantification: The percentage of expressing cells was calculated by dividing the number of nuclei labeled by the MyoG or MyoD antibody by the total amount of cells given by the Hoechst

staining in 3 independent replicates of each experimental condition. The nuclei were segmented and counted using the Cellpose software (Stringer et al., 2021).

Quantification of fusion index: First, the nuclei were segmented and counted using the Cellpose software (Stringer et al., 2021) together with a homemade python script to gain the total number of nuclei. Then, the fusion index was quantified by manually identifying the number of nuclei found in cells with at least two nuclei. The values were expressed as a percentage of the total number of nuclei per field of view.

Actin intensity quantification in a field of view

The quantification was made using the ImageJ v1.52 software (Schindelin et al., 2012). We measured the fluorescence intensity signal of the entire field of view every hour and plotted the mean intensity with stdDev calculated over all the pixel values of every field of view.

Automated single-cell tracking and quantification

Automatic nuclei speed was performed using the commercial software Imaris (v9.7.2, Oxford Instruments). We created a new "spots" layer on the nuclei label channel using the default Favorite Creation Parameters to track the spots over time, classify the spots, and object-object statistics. Next, we estimated the diameter of 8 µm and enabled background subtraction. These analyses allowed us to collect a large number of single-nuclei trajectories. While trajectories frequently fragment using this approach, they were sufficient to quantify the mean nuclei speed over time.

Semi-manual single-cell tracking

Semi-manual single-cell tracking was performed to obtain accurate trajectories for training and evaluating our machine-learning models. The time-lapse images were first converted to XML/hdf5 format using the BigDataViewer (v.6.2.1) FIJI plugin (Pietzsch et al., 2015; Schindelin et al., 2012). We then used the Mastodon FIJI plugin (Mastodon – a large-scale tracking and track-editing framework for large, multi-view images), for single-cell tracking and manual correction. We tracked cells that resided within the field of view throughout the entire experiment and included cells that fused into multinucleated fibers and cells that did not fuse within the experimental timeframe. To reduce the manual annotation load, tracks that contained

less tracking errors were prioritized for manual correction. Altogether, we collected 848 tracks for training (538 ERKi-treated cells; 310 DMSO-treated cells), 789 tracks, from an independent experiment, for testing (686 ERKi-treated cells; 103 DMSO-treated cells), and 410 tracks, from the perturbation experiment (202 P38i-treated cells; 208 ERKi+P38i-treated cells).

Preprocessing trajectories

We used OpenCV's CalcOpticalFlowFarneback, based on Gunner Farneback's method (Farnebäck, 2003), for image registration to correct erroneous offsets of the tracked cells' trajectories. For each pair of frames, we calculated the average offset and used the corresponding translation for registration.

Models training

The training pipeline implements the following steps.

1. Determining labels for training. We assigned ERKi-treated cells with the "differentiated" label in a time segment of 2.5 hours (hours 12.3-14.8) before the first fusion event was observed in the field of view. We decided not to label ERKi-treated cells as "undifferentiated" at the onset of the experiment because we did not know how early differentiation phenotypic signs appear. The increase in MyoG-positive cells during the first 6 hours of the experiment supports this decision. We assigned time segments of DMSO-treated cells with the "undifferentiated" label because their differentiation begins after more than the 23 hours of the experiment.

2. Partitioning single-cell trajectories to temporal segments. We partitioned trajectories of DMSO- and ERKi-treated cells to overlapping temporal segments (overlap lag = 5 minutes) in equal lengths of 2.5 hours each. Temporal segments' length was determined to match the time frame where we consider ERKi-treated cells as "differentiated". This step resulted in 16,636 DMSO-treated cells and 47,819 ERKi-treated cells temporal segments. For training, we labeled as "differentiated" ERKi-treated cells in the temporal segment of hours 12.3-14.8 and labeled as "undifferentiated" DMSO-treated cells in non-

overlapping temporal segments throughout the experiment. Overall, we extracted 468 undifferentiated and 268 differentiated temporal segments for training.

3. Extracting motility and actin features. We extracted single-cell motility and actin intensity time series from each temporal segment:

- Motility: We calculated the displacement of a single cell for each time point t, creating a two-dimensional vector: $displacement(t) = (x_t - x_{t-1}, y_t - y_{t-1})$
- Actin: We cropped a quantification window of size 32X32 µm around the center of each nucleus at each time point and calculated the minimum, maximum, mean, median, and standard deviation of the actin intensity within the window.

4. Extracting hundreds of single-cell time series features using the "tsfresh" python package (Christ et al., 2018). These features encoded properties of the temporal segments, such as temporal peaks, derivatives, and statistics. The tsfresh feature selection was based on the Benjamini-Yekutieli multiple test procedure (Benjamini & Yekutieli, 2001) to identify the most relevant features for characterizing the time series.

5. Training classifiers to distinguish between differentiated and undifferentiated cells. We trained random forest classifiers, which are considered effective with high dimensional and relatively small datasets (Breiman, 2001), as validated empirically on our data (Fig. SMLComparison). Hyperparameter tuning was performed using a grid search with a 5-fold cross-validation (motility classifier: {‘'max_depth': 12, 'min_samples_leaf': 1, 'n_estimators': 100}, actin intensity classifier: {'max_depth': 20, 'min_samples_leaf': 1, 'n_estimators': 200}).

6. Evaluating the trained classifies' performance. We assessed the discrimination performance of our motility/actin classifiers on an independent experiment that was not used for training. We partitioned time series to overlapping temporal segments (102,929 ERKi-treated cells segments, 7,214 DMSO-treated cells segments), selected temporal segments for evaluation as described above for 577 differentiated and 180 undifferentiated temporal segments, extracted motility and actin intensity time series, performed feature extraction using "tsfresh", and evaluated the performance of the

corresponding trained models. The AUC of the motility and the actin intensity classifiers were 0.8 and 0.81, correspondingly (Fig. 3E).

Inference of single cells differentiation trajectories

Each single cell trajectory was partitioned into overlapping temporal segments of 2.5 hours, with an overlapping lag of 5 minutes (one frame). We calculated motility & actin intensity time series, applied "tsfresh", selected features according to training, and applied the corresponding trained models on these feature vectors to retrieve a differentiation score for each segment defining single-cell differentiation trajectories.

Correlation of differentiation score with time

The correlation between the single-cell differentiation scores and time was computed through the critical time interval where differentiation occurred (7.5-14.5). We used the Spearman correlation coefficient as a measurement for the monotonic increase in differentiation along a trajectory.

Quantification of single cell predicted duration of the differentiation process

The *differentiation process duration* is a proxy for the time a single cell undergoes differentiation. The duration of the single-cell differentiation process was determined as the time passed from reaching a low, stable threshold to reaching a high stable threshold in the differentiation scores. The low, stable threshold was defined as the last time point of the longest sequence with differentiation scores that ranged between 0.2-0.3. The high stable threshold was defined as the first time point of the longest sequence with differentiation scores that ranged between 0.7-0.8. The differentiation process duration was calculated as the time passed between the low and high stable thresholds.

Simple single-cell measurements and corresponding classifiers

We calculated single-cell time series of the following measurements:

- Local density: the number of nuclei within a radius of 50 μm around the cell.

- Speed: $speed(t) = \sqrt{(x_t - x_{t-1})^2 + (y_t - y_{t-1})^2}$, where x_t, $y_t$are the nuclei (x, y)position at time t.
- Mean actin intensity: mean actin intensity in a quantification window of 32X32 µm around the nuclei.
- Persistence: The ratio between a single cell's displacement and its full path length. Persistence of 1 implies that the cell migrated in a straight line.

For each measurement, and for all four together, we trained random forest classifiers with the mean value in each temporal segment to discriminate between undifferentiated and differentiated cells. We evaluated the discrimination performance of each of the five classifiers as described above.

Quantification of single-cell terminal differentiation time:

The *terminal differentiation time* of a single cell is an estimation based on the first time of the longest sequence of differentiation scores that are higher than a threshold value of 0.78 (to avoid local peaks).

Manual annotation of fusion events timing

68 nuclei from 6 fibers were backtracked to the frame when they fused into the fiber syncytium (Fig. S13).

Statistical analysis

Pearson correlation (scipy.stats.pearsonr function) was used to assess the correlation between the terminal differentiation time and fusion since we assumed a linear correlation between them (Fig. 4D). Spearman correlation (using scipy.stats.pearsonr function) was used for correlating the monotonic increase in the differentiation trajectories with time. D'Agostino's K-squared test (using scipy.stats.normaltest) was used to determine the normality of distributions: duration of the differentiation process, terminal differentiation time, fusion time, and duration between differentiation and fusion.

Software and data availability

We are currently organizing our source code and will make it publically available as soon as possible (before journal publications).

Supplementary information:

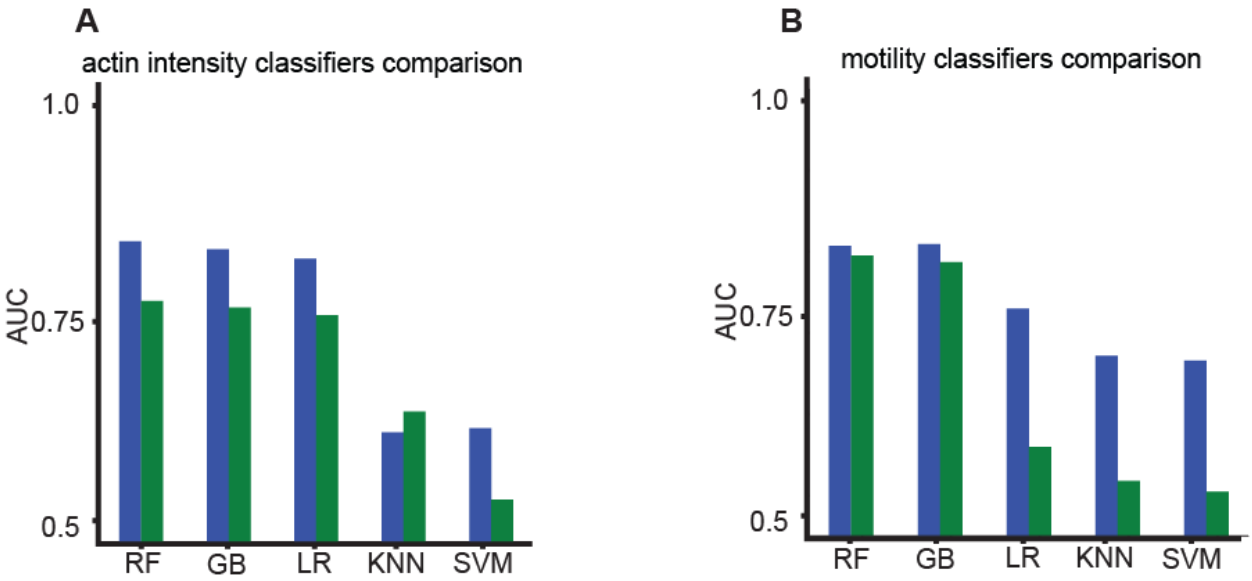

Figure S1. Comparison of classification algorithms
(A-B) Area under the receiver operating characteristic (ROC) curve (AUC) for classifiers trained with actin intensity(A) and motility (B) time series, using random forest (RF), gradient boosting (GB), logistic regression (LR), k-nearest neighbors (KNN), and support vector machines (SVM). Blue/green – flipped train/test experiments. Average AUCs for actin intensity classifiers were 0.78 (RF), 0.77 (GB), 0.76 (LR), 0.59 (KNN), 0.54 (SVM). Average AUCs for motility classifiers were 0.8 (RF), 0.8 (GB), 0.64 (LR), 0.59 (KNN), 0.59 (SVM).

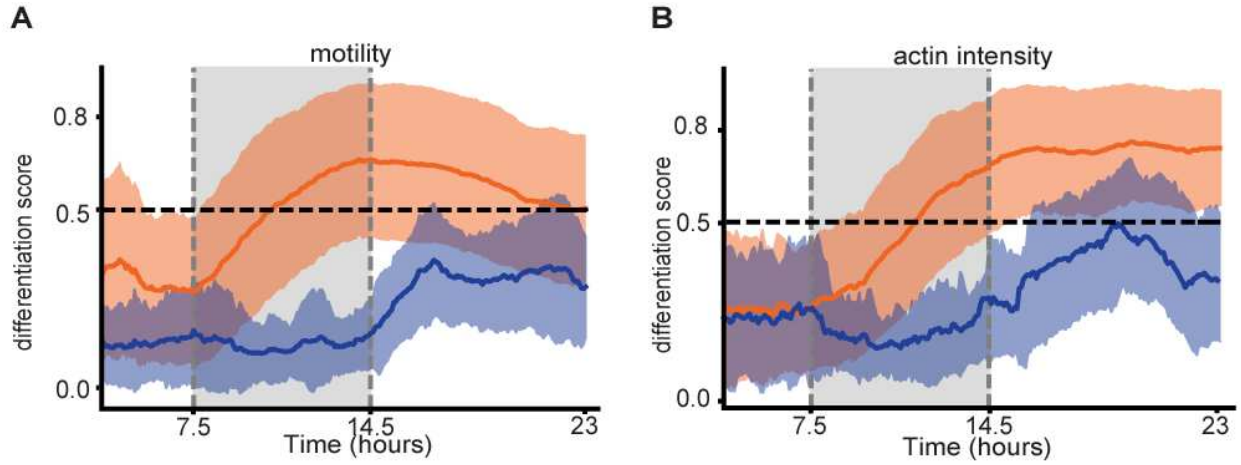

Figure S2. Differentiation scores over time for the entire experiment

(A-B) Mean (solid line) and standard deviation (shade) of the differentiation score over time of ERKi- (orange) and DMSO- (blue) treated cells using the motility (A) and the actin intensity (B) classifiers. Dashed vertical gray rectangle highlights the time interval of 7.5-14.5 hours, where both models predicted the differentiation occurs. The increase of the untreated cells' differentiation score in concurrence with unchanged (actin) or reduced (motility) scores for ERKi-treated cells around 14.5 hours could be due to altered motility/actin dynamics of untreated cells in denser microenvironments and due to differentiated ERKi-treated cells undergoing fusion.

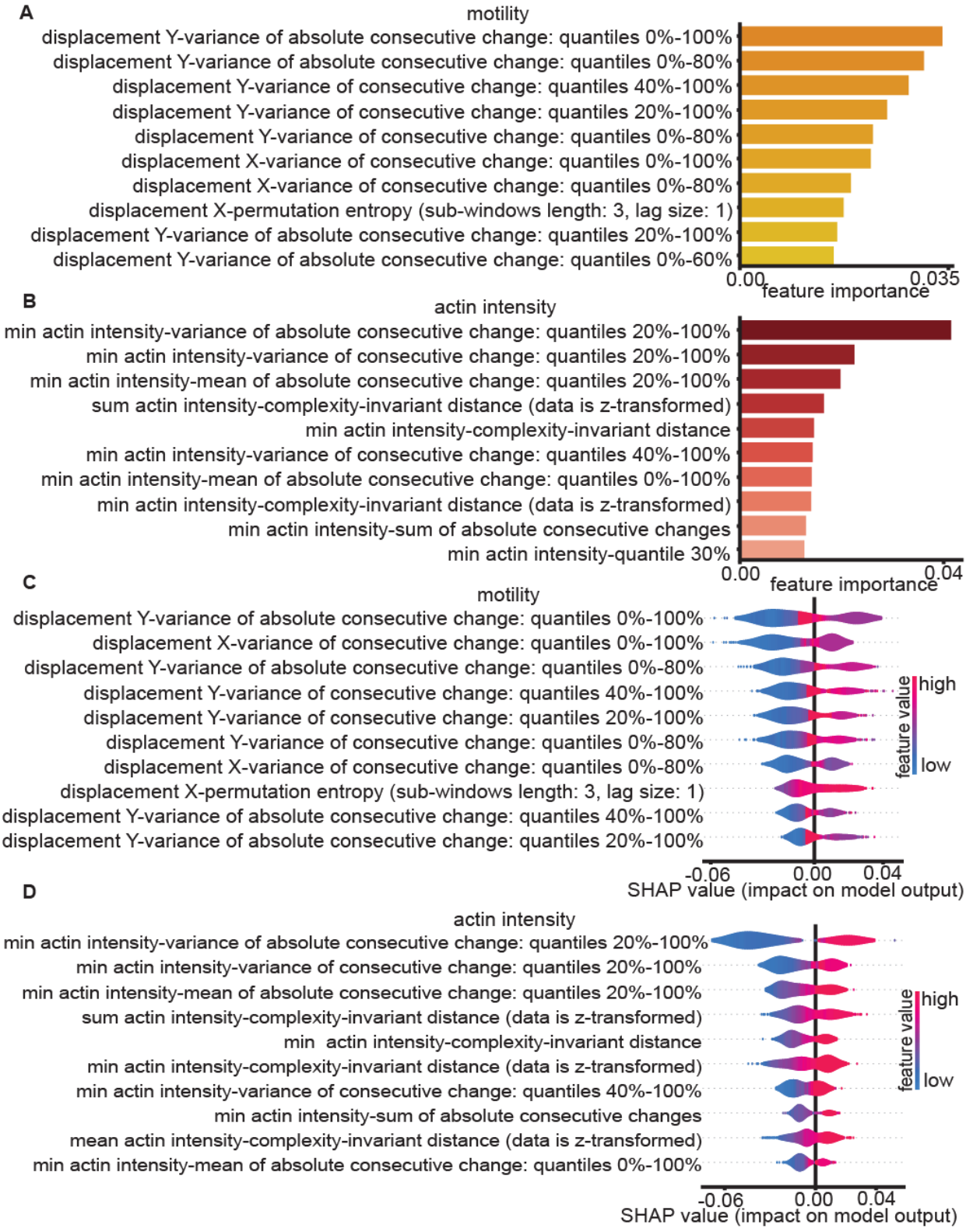

Figure S3. Random forests feature importance

Top ten features most relevant for differentiation classification using random forest classifiers' importance (A-B) and SHapley Additive exPlanation (SHAP) (C-D). Both approaches find very similar important features: variance of consecutive change in displacement, permutation entropy of displacement, variance of consecutive change in actin intensity, complexity-invariant distance of actin intensity and sum of absolute consecutive changes in actin intensity. **(A-B)** Feature importance of random forest classifiers trained to discriminate undifferentiated/differentiated cell states, on features extracted from motility (yellow) and actin intensity (red), time series using "tsfresh" package. The 10 most important features are shown. **(C-D)** SHAP summary plots of motility (C) and actin intensity (D) classifiers, produced by the SHAP python package (Lundberg & Lee, 2017). The plot illustrates the feature relevance and combines feature attributions to the model's predictive performance. Color is dependent on the feature values. The 10 most important features are shown.

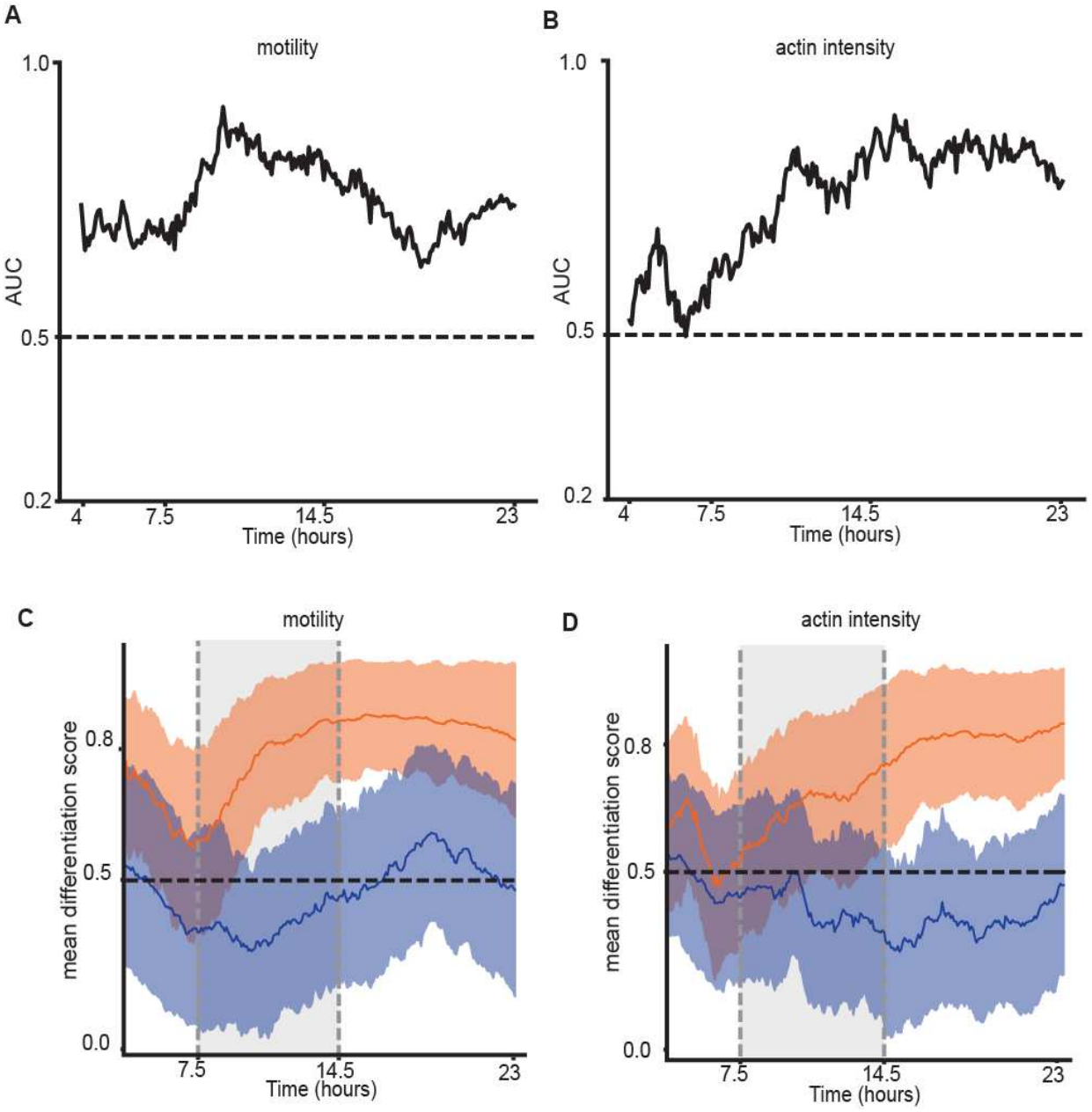

Figure S4. Inference of differentiation trajectories - flipped experiments for train/test
(A-B) Classification performance over time for the entire experiment. Area under the receiver operating characteristic (ROC) curve (AUC) over time for classifiers trained with motility (B) and actin intensity (C) time-series. The AUC was calculated for 736 cells from an independent experiment. Classification performance of a random model (AUC = 0.5) is marked with a dashed horizontal line. Compare with Fig. 2B-C. **(C-D)** Mean (solid line) and standard deviation (shade) of the differentiation score over time of ERKi- (orange) and DMSO- (blue) treated cells using the motility (B) and the actin intensity (C) classifiers over time for the entire experiment. Dashed vertical gray rectangle highlights the time interval of 7.5-14.5 hours, where both models predicted the differentiation occurs. Compare with Fig. S2.

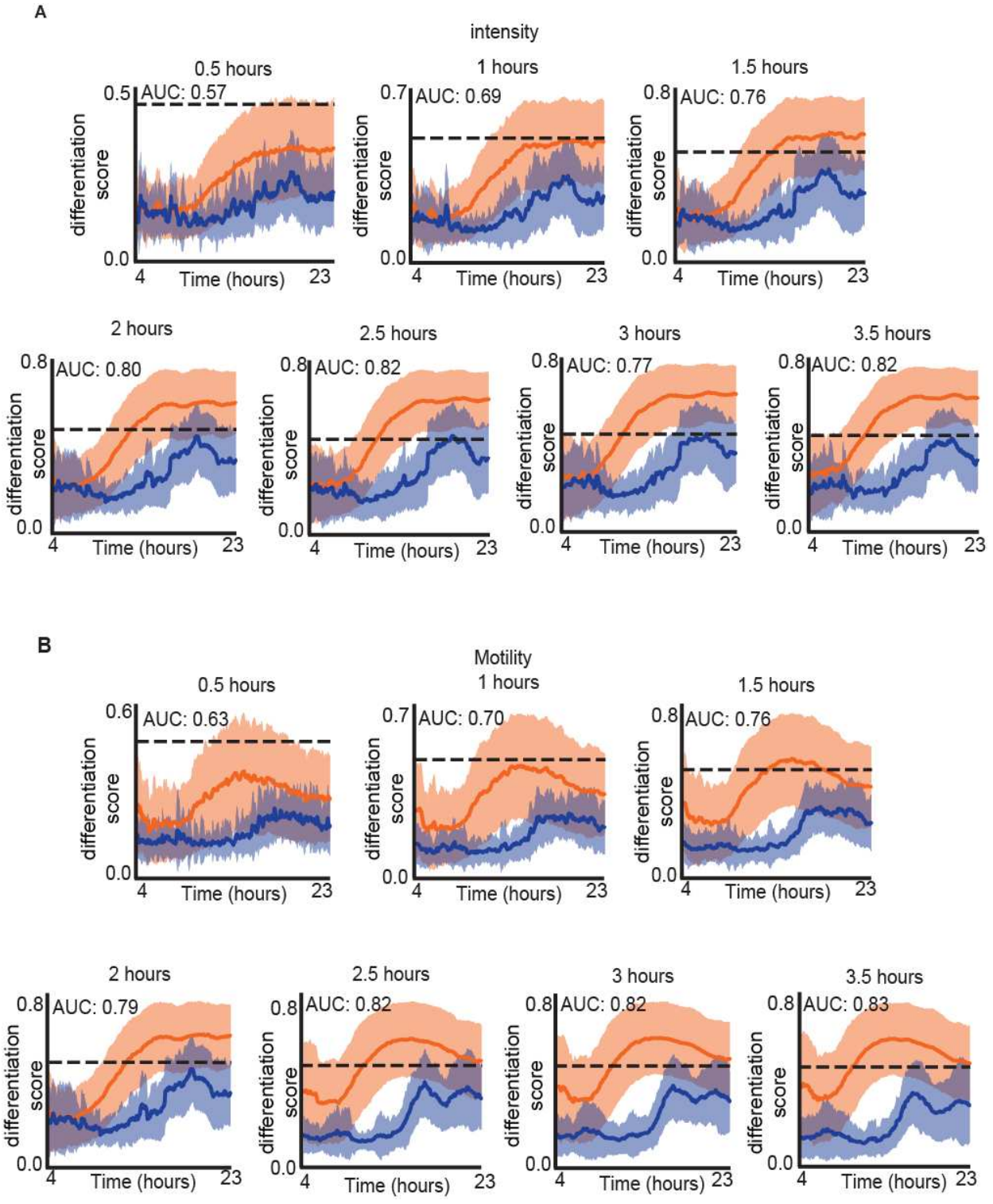

Figure S5. Classification sensitivity analysis: temporal segment size

(A-B) Mean (solid line) and standard deviation (shade) of the differentiation score over time of ERKi- (orange) and DMSO- (blue) treated cells using the motility (B) and the actin intensity (C) classifiers, trained with different sizes of temporal segment. Temporal segment's size (in hours) is shown above each

graph. Corresponding AUCs are reported in the figure. The temporal segment size for both classifiers was 2.5 hours.

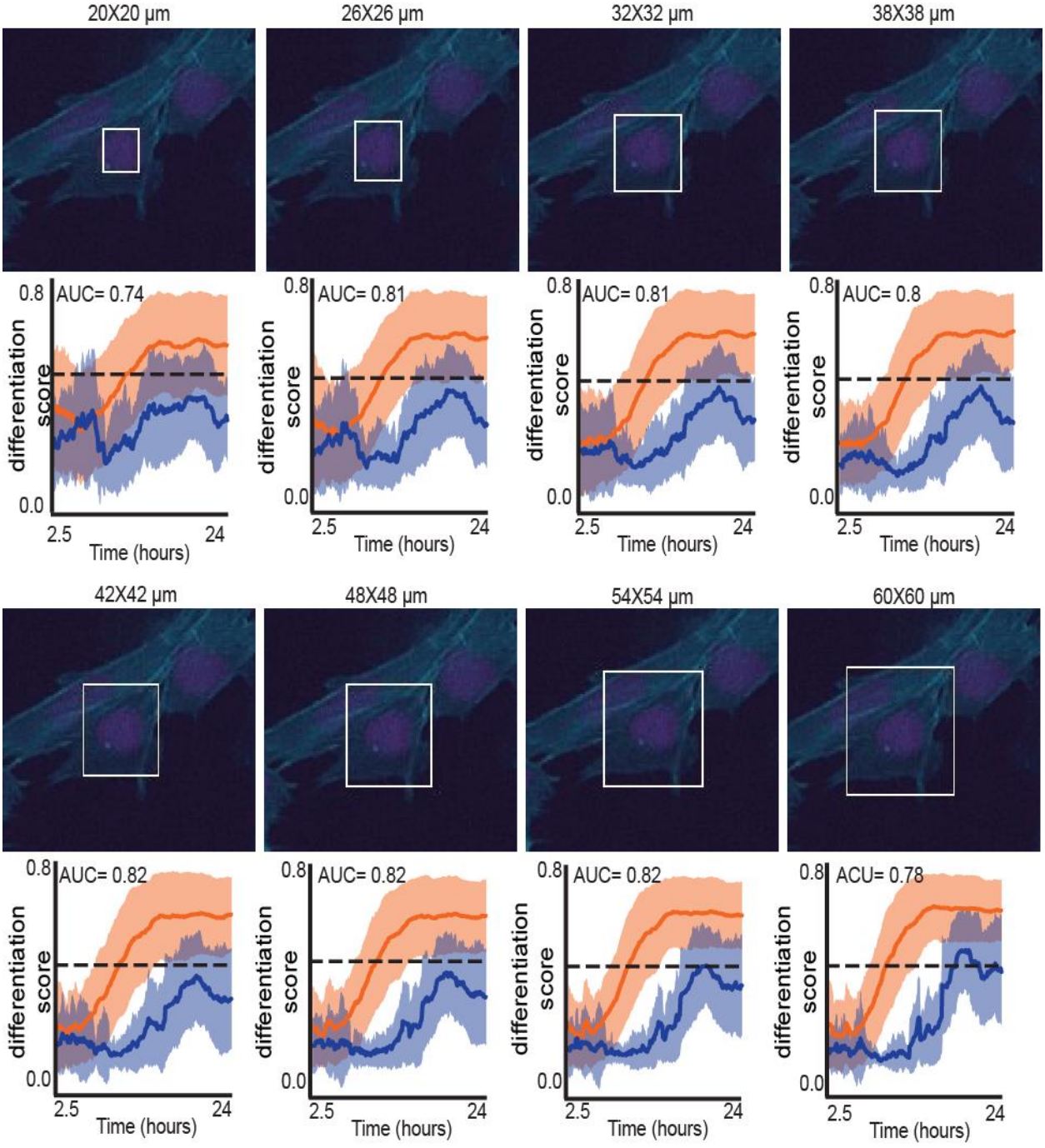

Figure S6. Classification sensitivity analysis: actin intensity quantification window size
Top: an illustration of the actin quantification window size. Bottom: Mean (solid line) and standard deviation (shade) of the differentiation score over time of ERKi- (orange) and DMSO- (blue) treated cells

using the actin intensity classifier, trained using these window sizes. Corresponding AUCs are reported in the figure.

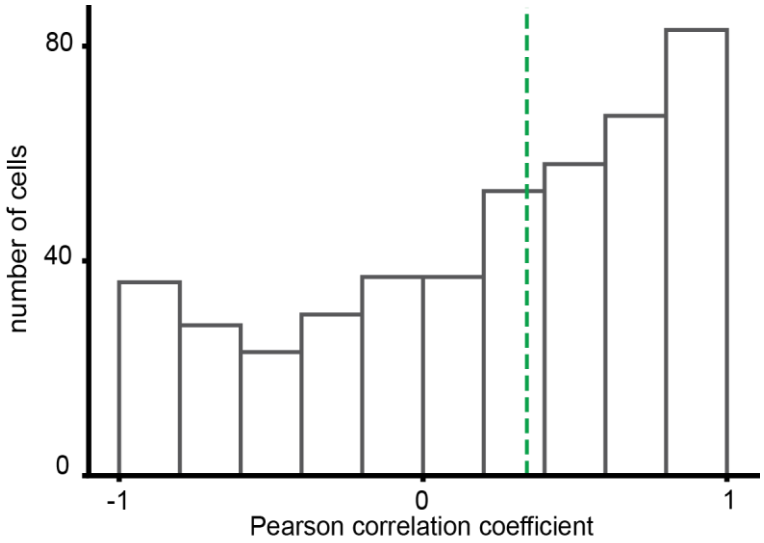

Figure S7: Motility and actin intensity models agree on monotonically increasing differentiation trajectories

Distribution of single cells agreement between the predictions of motility and actin intensity classifiers, determined by the Pearson correlation coefficient of the correlation between the inferred trajectories in the differentiation time interval of 7.5-14.5 hours. The agreement was assessed for 574 ERKi-treated cells and 81 DMSO-treated cells. Median Pearson correlation coefficient (green dashed line) was 0.34.

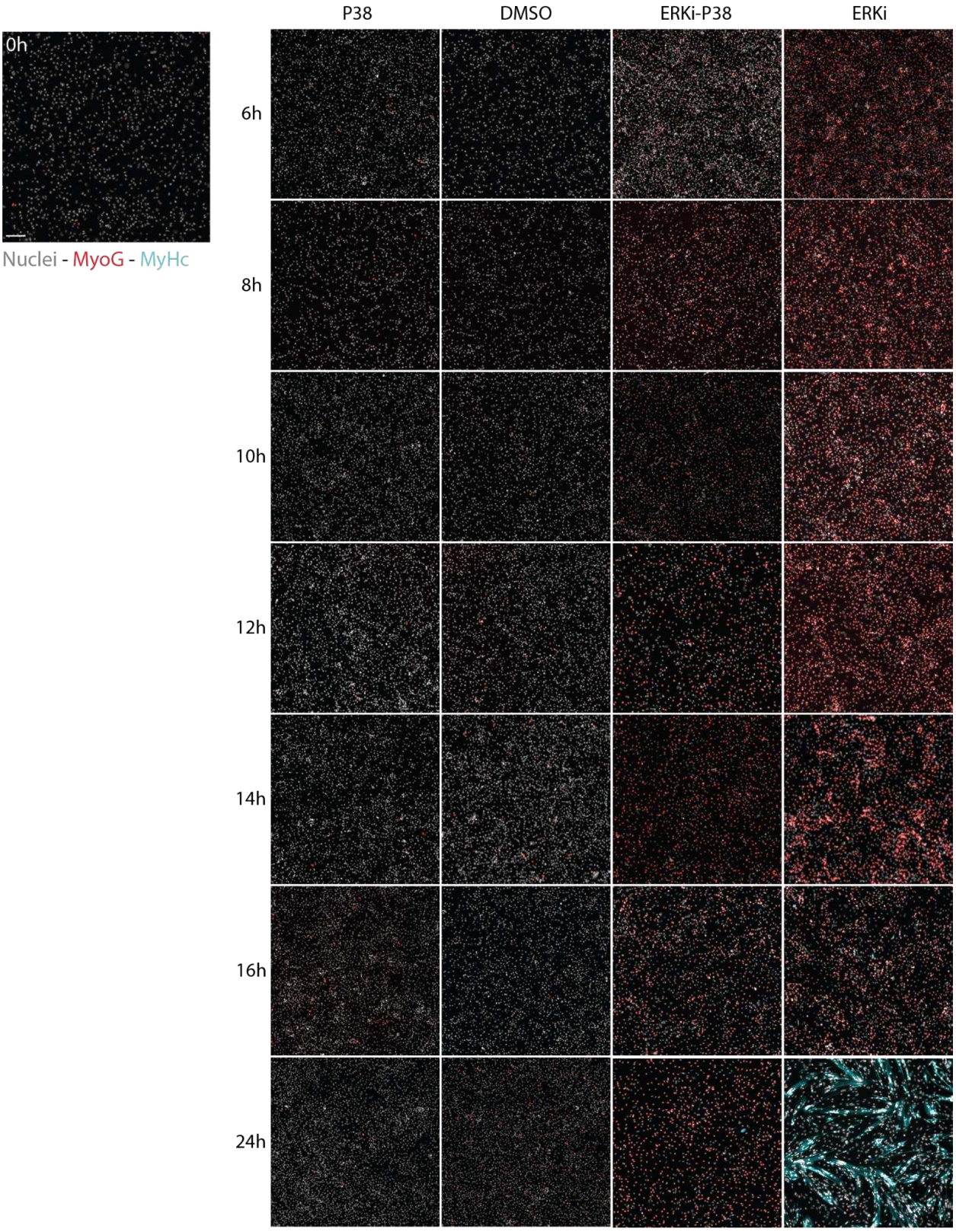

Figure S8. Immunofluorescence staining of MyoG and MyHC

Representative immunofluorescence (IF) images of myoblasts at 0,6,8,10,12,14,16, 24 hours after treatment with DMSO, P38i 5 μM or ERKi 1 μM or the combination of ERki-P38i. Cells were stained using anti-MyoG (red) and anti-MyHC (cyan) (methods), and the nuclear dye Hoechst 33342 (gray). Magnification 5x, Scale bar: 100 μm.

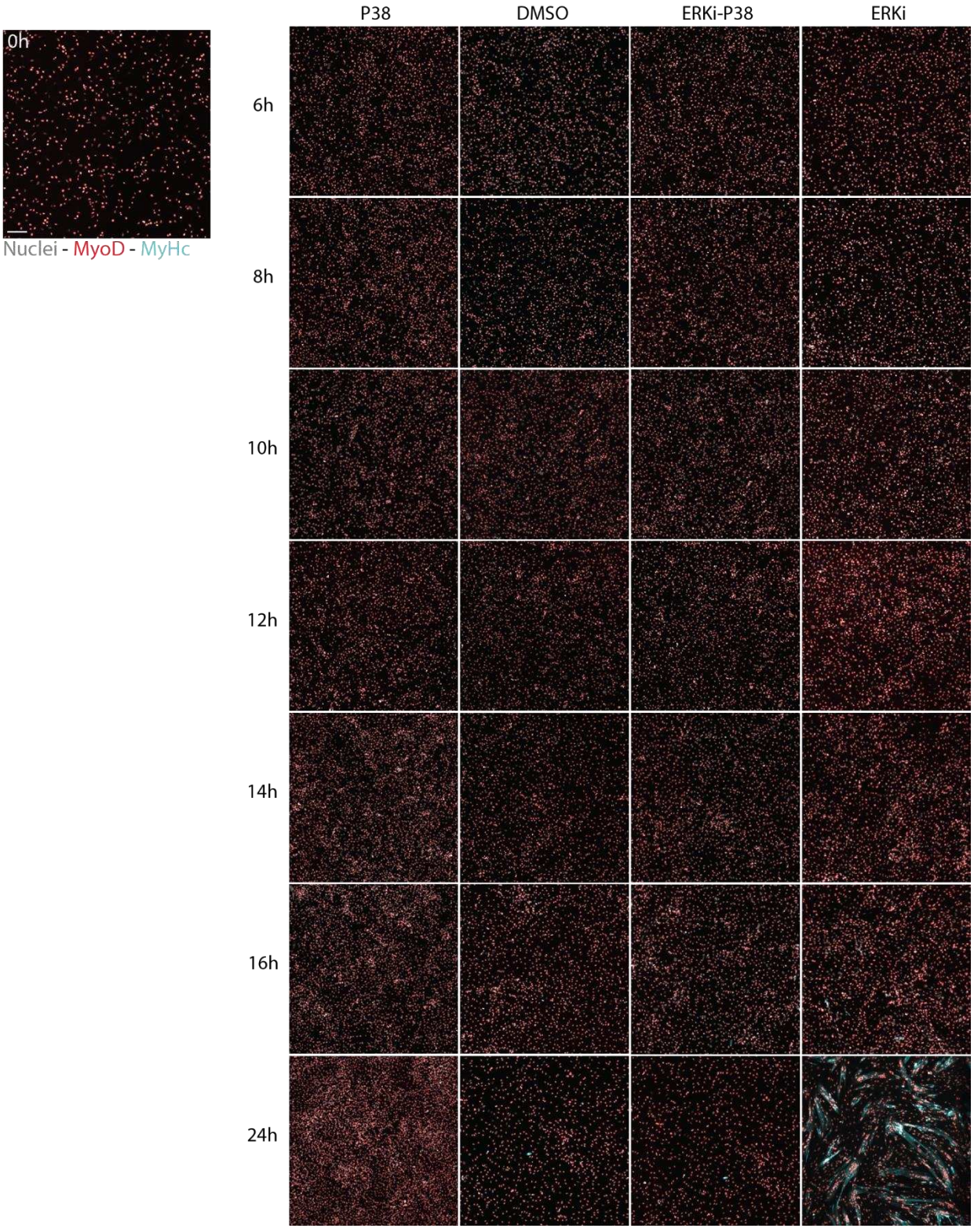

Figure S9. Immunofluorescence staining of MyoD and MyHC

Representative immunofluorescence (IF) images of myoblasts at 0,6,8,10,12,14,16, 24 hours after treatment with DMSO, P38i 5 μM or ERKi 1 μM or the combination of ERki-P38i. Cells were stained

using anti-MyoG (red) and anti-MyHC (cyan) (methods), and the nuclear dye Hoechst 33342 (gray). Magnification 5x, Scale bar: 100 μm.

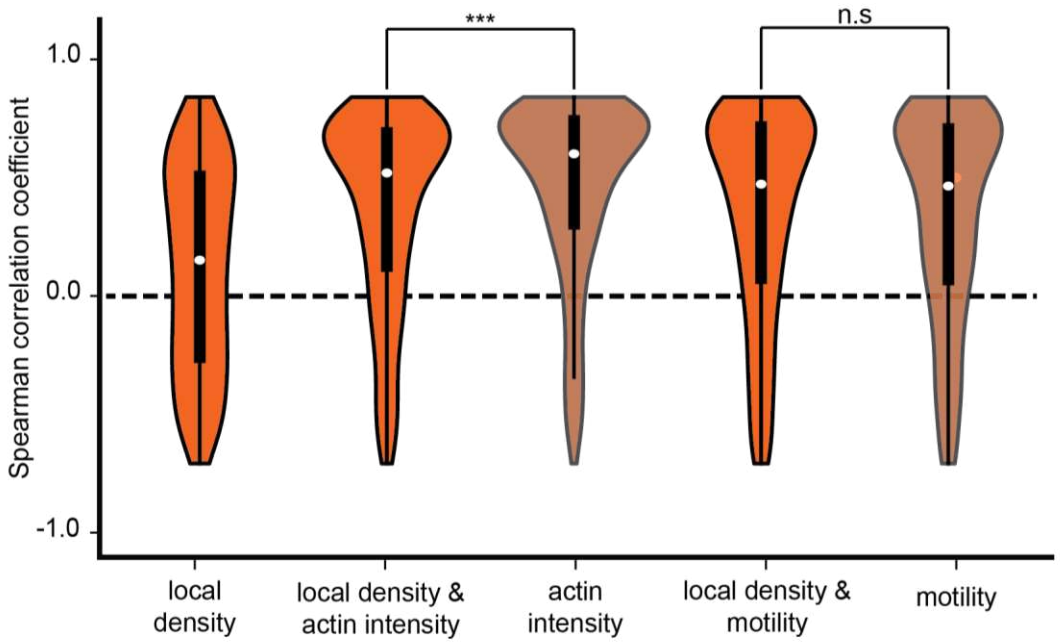

Figure S10. Local density does not improve quantification of the continuous differentiation state
Distribution of single cell correlation between the differentiation score and time for classifiers trained using features that include or exclude local density. Dashed horizontal line shows no correlation. Median values (shown in white) were 0.09 (local density), 0.62 (local density + actin intensity), 0.67 (actin intensity), 0.53 (local density + motility), 0.53 (motility). The correlations of the actin intensity classifier were higher without the local density feature (Wilcoxon rank sign test p-value = $5.7 * 10^{-10}$), the correlations of the motility classifier were not improved by including the local density feature. N = 675 cells. *** - p-value < 0.0001, n.s – not significant.

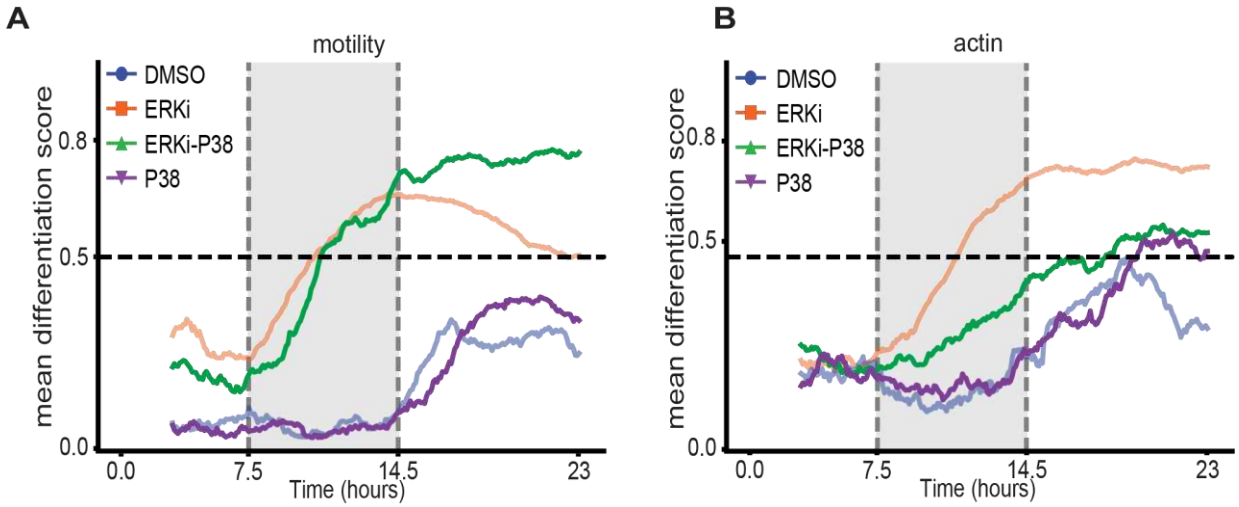

Figure S11: Differentiation scores for P38i perturbation

(A-B) Mean differentiation score over time of ERKi- (orange), DMSO- (blue), ERKi+P38i- (green) and P38i- (purple) treated cells using the motility (A) and actin intensity (B) classifiers. Dashed vertical gray rectangle highlights the differentiation time interval of 7.5-14.5 hours. ERKi- and DMSO- treated cells differentiation scores are the same as shown in Fig. 5A-B. Since co-treated cells undergo differentiation but not fusion, the differentiation score did not decrease after 14.5 hours, unlike ERKi-treated cells that begin to massively fuse at these times and thus change their motility and actin dynamics.

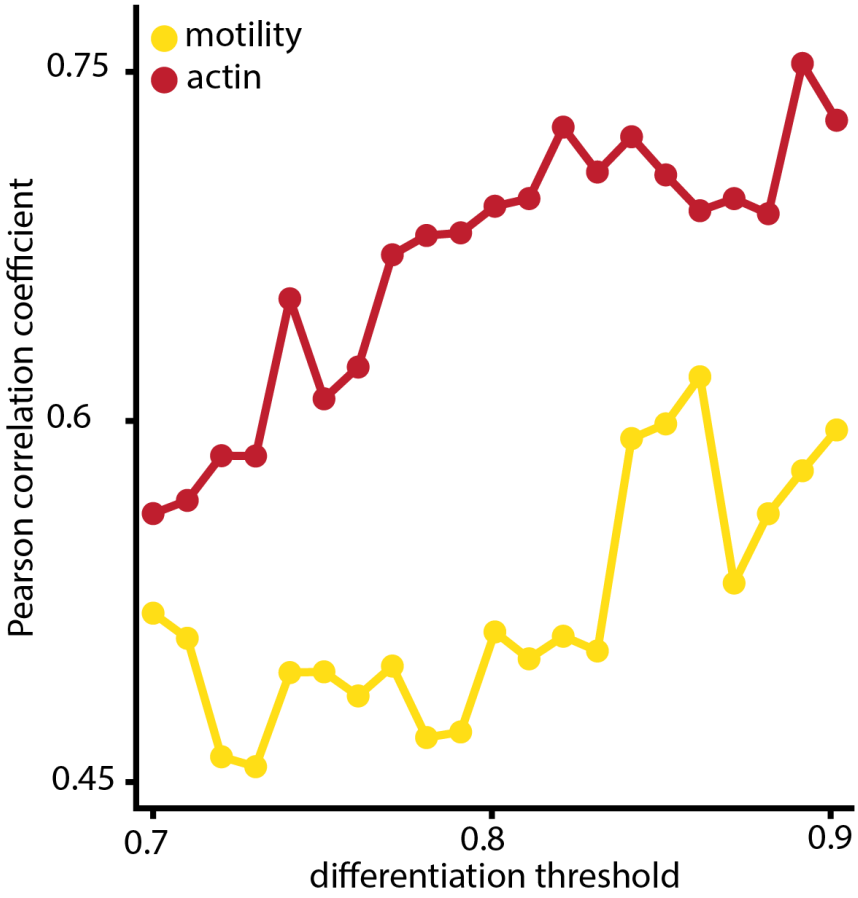

Figure S12. Sensitivity analysis: threshold for terminal differentiation
Pearson correlation coefficient of the correlation between the (predicted) terminal differentiation time and the manually annotated fusion time, for different terminal differentiation thresholds. The number of cells that are identified as terminally differentiated depends on the threshold, thus as the threshold increases- the number of identified cells decreases.

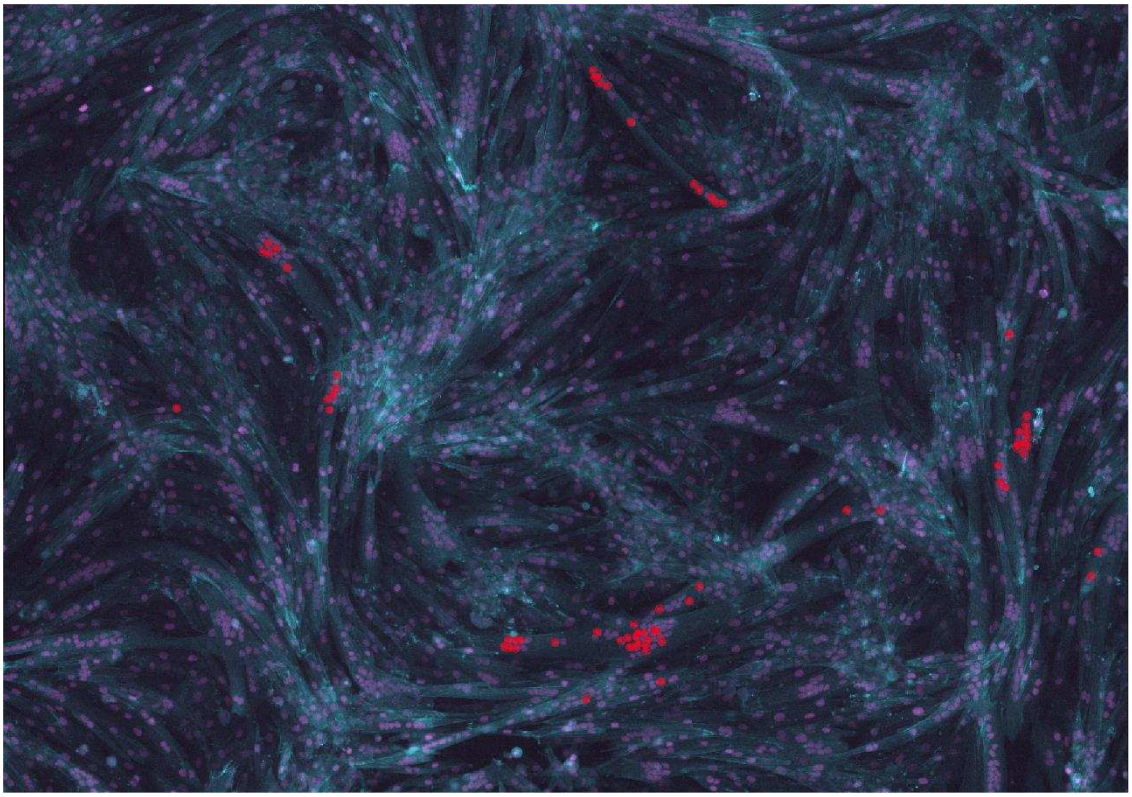

Figure S13: Nuclei fusion manual annotation.
Overlay image showing nuclei in fibers, which were selected for backtracking. All nuclei (magenta) and actin (cyan) are shown.

Video S1: Proliferating (DMSO) versus Differentiating (ERKi) myoblasts.
Actin and nuclear reporters (LifeAct-GFP/ nTnG+/+) lineage traced primary myoblasts showing proliferating myoblasts (DMSO-treated myoblasts; left) and differentiating myoblasts (ERKi-treated myoblasts; right). Time lapse images were acquired using a 10× objective with a 5 minute interval between frames. Imaging started 1 hour and 30 minutes after treatment. (Time scale: hh:mm). Scale bar 100 µm. Linear adjustments to brightness and contrast were made using ImageJ.

Video S2: A video of representative single cell trajectories fusing into a single myofiber.
Cells were tracked and manually edited using Mastodon FIJI plugin (*mastodon: Mastodon – a large-scale tracking and track-editing framework for large, multi-view images*, n.d.).

Video S3: Proliferating (P38i) versus Differentiating without fusion (ERKi-P38i) myoblasts.
Actin and nuclear reporters (LifeAct-GFP/ nTnG+/+) lineage traced primary myoblasts showing proliferating myoblasts (P38i-treated myoblasts; left) and differentiating myoblasts without fusion (ERKi-P38i-treated myoblasts; right). Time lapse images were acquired using a 10× objective with a 5 minute interval between frames. Imaging started 1 hour and 30 minute after treatment. (Time scale: hh:mm). Scale bar 100 µm. Linear adjustments to brightness and contrast were made using ImageJ

Funding and Acknowledgments

This research was supported by the Israeli Council for Higher Education (CHE) via the Data Science Research Center, Ben-Gurion University of the Negev, Israel (to AZ), and by the Wellcome Leap Delta Tissue program (to AZ). This project also received funding from the European Research Council (ERC StG # 851080 to O.A.). O.A. also acknowledges funding from the David Barton Center for Research on the Chemistry of Life and the Ruth and Herman Albert Scholarship Program for New Scientists. O.A. is an incumbent of the Miriam Berman Presidential Development Chair. We thank Shahar Golan for critically reading the manuscript.

Author Contribution

AZ and OA conceived the study. GZ and AH designed the experimental assay and performed all experiments. AS developed analytic tools, analyzed, and interpreted the data with the help of RM. AS, GZ, RM and KH curated and annotated data. AS, OA, and AZ drafted the manuscript. OA and AZ mentored the authors. All authors wrote and edited the manuscript and approved its content.

Competing Financial Interests

OA is a co-founder of ProFuse technologies LTD.

References

Abmayr, S. M., & Pavlath, G. K. (2012). Myoblast fusion: lessons from flies and mice. *Development* , *139*(4), 641–656. https://doi.org/10.1242/dev.068353

Bains, W., Ponte, P., Blau, H., & Kedes, L. (1984). Cardiac actin is the major actin gene product in skeletal muscle cell differentiation in vitro. *Molecular and Cellular Biology*, *4*(8), 1449–1453. https://doi.org/10.1128/mcb.4.8.1449-1453.1984

Benjamini, Y., & Yekutieli, D. (2001). The Control of the False Discovery Rate in Multiple Testing under Dependency. *Annals of Statistics*, *29*(4), 1165–1188. http://www.jstor.org/stable/2674075

Bentzinger, C. F., Wang, Y. X., & Rudnicki, M. A. (2012). Building muscle: molecular regulation of myogenesis. *Cold Spring Harbor Perspectives in Biology*, *4*(2). https://doi.org/10.1101/cshperspect.a008342

Bischoff, R. (1986). Proliferation of muscle satellite cells on intact myofibers in culture. *Developmental Biology*, *115*(1), 129–139. https://doi.org/10.1016/0012-1606(86)90234-4

Breiman, L. (2001). Random Forests. *Machine Learning*, *45*(1), 5–32. https://doi.org/10.1023/A:1010933404324

Buggenthin, F., Buettner, F., Hoppe, P. S., Endele, M., Kroiss, M., Strasser, M., Schwarzfischer, M., Loeffler, D., Kokkaliaris, K. D., Hilsenbeck, O., Schroeder, T., Theis, F. J., & Marr, C. (2017). Prospective identification of hematopoietic lineage choice by deep learning. *Nature Methods*, *14*(4), 403–406. https://doi.org/10.1038/nmeth.4182

Choi, H. J., Wang, C., Pan, X., Jang, J., Cao, M., Brazzo, J. A., 3rd, Bae, Y., & Lee, K. (2021). Emerging machine learning approaches to phenotyping cellular motility and morphodynamics. *Physical Biology*, *18*(4). https://doi.org/10.1088/1478-3975/abffbe

Christ, M., Braun, N., Neuffer, J., & Kempa-Liehr, A. W. (2018). Time Series FeatuRe Extraction on basis of Scalable Hypothesis tests (tsfresh – A Python package). *Neurocomputing*, *307*, 72–77. https://doi.org/10.1016/j.neucom.2018.03.067

Copperman, J., Gross, S. M., Chang, Y. H., Heiser, L. M., & Zuckerman, D. M. (2021). Morphodynamical cell-state description via live-cell imaging trajectory embedding. In *bioRxiv* (p. 2021.10.07.463498). https://doi.org/10.1101/2021.10.07.463498

Eigler, T., Zarfati, G., Amzallag, E., Sinha, S., Segev, N., Zabary, Y., Zaritsky, A., Shakked, A., Umansky, K.-B., Schejter, E. D., Millay, D. P., Tzahor, E., & Avinoam, O. (2021). ERK1/2 inhibition promotes robust myotube growth via CaMKII activation resulting in myoblast-to-myotube fusion. *Developmental Cell*, *56*(24), 3349-3363.e6. https://doi.org/10.1016/j.devcel.2021.11.022

Eulenberg, P., Köhler, N., Blasi, T., Filby, A., Carpenter, A. E., Rees, P., Theis, F. J., & Wolf, F. A. (2017). Reconstructing cell cycle and disease progression using deep learning. *Nature Communications*, *8*(1), 463. https://doi.org/10.1038/s41467-017-00623-3

Farnebäck, G. (2003). Two-Frame Motion Estimation Based on Polynomial Expansion. *Image Analysis*, 363–370. https://doi.org/10.1007/3-540-45103-X_50

Fischer, U., Ludwig, N., Raslan, A., Meier, C., & Meese, E. (2016). Gene amplification during myogenic differentiation. *Oncotarget*, *7*(6), 6864–6877. https://doi.org/10.18632/oncotarget.6845

Gardner, S., Gross, S. M., David, L. L., Klimek, J. E., & Rotwein, P. (2015). Separating myoblast differentiation from muscle cell fusion using IGF-I and the p38 MAP kinase inhibitor SB202190. *American Journal of Physiology. Cell Physiology*, *309*(7), C491-500. https://doi.org/10.1152/ajpcell.00184.2015

Goglia, A. G., Wilson, M. Z., Jena, S. G., Silbert, J., Basta, L. P., Devenport, D., & Toettcher, J. E. (2020). A Live-Cell Screen for Altered Erk Dynamics Reveals Principles of Proliferative Control. *Cell Systems*, *10*(3), 240-253.e6. https://doi.org/10.1016/j.cels.2020.02.005

Gut, G., Tadmor, M. D., Pe'er, D., Pelkmans, L., & Liberali, P. (2015). Trajectories of cell-cycle progression from fixed cell populations. *Nature Methods*, *12*(10), 951–954. https://doi.org/10.1038/nmeth.3545

Hernández-Hernández, J. M., García-González, E. G., Brun, C. E., & Rudnicki, M. A. (2017). The myogenic regulatory factors, determinants of muscle development, cell identity and regeneration. *Seminars in Cell & Developmental Biology*, *72*, 10–18. https://doi.org/10.1016/j.semcdb.2017.11.010

Hurme, T., & Kalimo, H. (1992). Activation of myogenic precursor cells after muscle injury. *Medicine and Science in Sports and Exercise*, *24*(2), 197–205. https://www.ncbi.nlm.nih.gov/pubmed/1549008

Jacques, M.-A., Dobrzyński, M., Gagliardi, P. A., Sznitman, R., & Pertz, O. (2021). CODEX, a neural network approach to explore signaling dynamics landscapes. *Molecular Systems Biology*, *17*(4), e10026. https://doi.org/10.15252/msb.202010026

Jena, S. G., Goglia, A. G., & Engelhardt, B. E. (2022). Towards "end-to-end" analysis and understanding of biological timecourse data. *Biochemical Journal*, *479*(11), 1257–1263. https://doi.org/10.1042/BCJ20220053

Kimmel, J. C., Chang, A. Y., Brack, A. S., & Marshall, W. F. (2018). Inferring cell state by quantitative motility analysis reveals a dynamic state system and broken detailed balance. *PLoS Computational Biology*, *14*(1), e1005927.

https://doi.org/10.1371/journal.pcbi.1005927

Lepper, C., Partridge, T. A., & Fan, C.-M. (2011). An absolute requirement for Pax7-positive satellite cells in acute injury-induced skeletal muscle regeneration. *Development* , *138*(17), 3639–3646. https://doi.org/10.1242/dev.067595

Lundberg, S., & Lee, S.-I. (2017). A unified approach to interpreting model predictions. In *arXiv [cs.AI]*. arXiv. https://proceedings.neurips.cc/paper/2017/hash/8a20a8621978632d76c43dfd28b67767-Abstract.html

mastodon: Mastodon – a large-scale tracking and track-editing framework for large, multi-view images. (n.d.). Github. Retrieved December 15, 2022, from https://github.com/mastodon-sc/mastodon

Mayr, C. H., Simon, L. M., Leuschner, G., Ansari, M., Schniering, J., Geyer, P. E., Angelidis, I., Strunz, M., Singh, P., Kneidinger, N., Reichenberger, F., Silbernagel, E., Böhm, S., Adler, H., Lindner, M., Maurer, B., Hilgendorff, A., Prasse, A., Behr, J., … Schiller, H. B. (2021). Integrative analysis of cell state changes in lung fibrosis with peripheral protein biomarkers. *EMBO Molecular Medicine*, *13*(4), e12871. https://doi.org/10.15252/emmm.202012871

Morris, E. J., Jha, S., Restaino, C. R., Dayananth, P., Zhu, H., Cooper, A., Carr, D., Deng, Y., Jin, W., Black, S., Long, B., Liu, J., Dinunzio, E., Windsor, W., Zhang, R., Zhao, S., Angagaw, M. H., Pinheiro, E. M., Desai, J., … Samatar, A. A. (2013). Discovery of a novel ERK inhibitor with activity in models of acquired resistance to BRAF and MEK inhibitors. *Cancer Discovery*, *3*(7), 742–750. https://doi.org/10.1158/2159-8290.CD-13-0070

Pietzsch, T., Saalfeld, S., Preibisch, S., & Tomancak, P. (2015). BigDataViewer: visualization and processing for large image data sets. *Nature Methods*, *12*(6), 481–483. https://doi.org/10.1038/nmeth.3392

Prigge, J. R., Wiley, J. A., Talago, E. A., Young, E. M., Johns, L. L., Kundert, J. A., Sonsteng, K. M., Halford, W. P., Capecchi, M. R., & Schmidt, E. E. (2013). Nuclear double-fluorescent reporter for in vivo and ex vivo analyses of biological transitions in mouse nuclei. *Mammalian Genome: Official Journal of the International Mammalian Genome Society*. https://doi.org/10.1007/s00335-013-9469-8

Rappez, L., Rakhlin, A., Rigopoulos, A., Nikolenko, S., & Alexandrov, T. (2020). DeepCycle reconstructs a cyclic cell cycle trajectory from unsegmented cell images using convolutional neural networks. *Molecular Systems Biology*, *16*(10), e9474. https://doi.org/10.15252/msb.20209474

Riedl, J., Crevenna, A. H., Kessenbrock, K., Yu, J. H., Neukirchen, D., Bista, M., Bradke, F., Jenne, D., Holak, T. A., Werb, Z., Sixt, M., & Wedlich-Soldner, R. (2008). Lifeact: a versatile marker to visualize F-actin. *Nature Methods*, *5*(7), 605–607. https://doi.org/10.1038/nmeth.1220

Schindelin, J., Arganda-Carreras, I., Frise, E., Kaynig, V., Longair, M., Pietzsch, T., Preibisch, S., Rueden, C., Saalfeld, S., Schmid, B., Tinevez, J.-Y., White, D. J., Hartenstein, V., Eliceiri, K., Tomancak, P., & Cardona, A. (2012). Fiji: an open-source platform for biological-image analysis. *Nature Methods*, *9*(7), 676–682. https://doi.org/10.1038/nmeth.2019

Schmidt, M., Schüler, S. C., Hüttner, S. S., von Eyss, B., & von Maltzahn, J. (2019). Adult stem cells at work: regenerating skeletal muscle. *Cellular and Molecular Life Sciences: CMLS*,

76(13), 2559–2570. https://doi.org/10.1007/s00018-019-03093-6

Schroeder, T. (2011). Long-term single-cell imaging of mammalian stem cells. *Nature Methods*, *8*(4 Suppl), S30-5. https://doi.org/10.1038/nmeth.1577

Singh, K., & Dilworth, F. J. (2013). Differential modulation of cell cycle progression distinguishes members of the myogenic regulatory factor family of transcription factors. *The FEBS Journal*, *280*(17), 3991–4003. https://doi.org/10.1111/febs.12188

Stallaert, W., Kedziora, K. M., Taylor, C. D., Zikry, T. M., Ranek, J. S., Sobon, H. K., Taylor, S. R., Young, C. L., Cook, J. G., & Purvis, J. E. (2022). The structure of the human cell cycle. *Cell Systems*, *13*(1), 103. https://doi.org/10.1016/j.cels.2021.12.006

Stringer, C., Wang, T., Michaelos, M., & Pachitariu, M. (2021). Cellpose: a generalist algorithm for cellular segmentation. *Nature Methods*, *18*(1), 100–106. https://doi.org/10.1038/s41592-020-01018-x

Stumpf, P. S., Smith, R. C. G., Lenz, M., Schuppert, A., Müller, F.-J., Babtie, A., Chan, T. E., Stumpf, M. P. H., Please, C. P., Howison, S. D., Arai, F., & MacArthur, B. D. (2017). Stem Cell Differentiation as a Non-Markov Stochastic Process. *Cell Systems*, *5*(3), 268-282.e7. https://doi.org/10.1016/j.cels.2017.08.009

Szkalisity, A., Piccinini, F., Beleon, A., Balassa, T., Varga, I. G., Migh, E., Molnar, C., Paavolainen, L., Timonen, S., Banerjee, I., Ikonen, E., Yamauchi, Y., Ando, I., Peltonen, J., Pietiäinen, V., Honti, V., & Horvath, P. (2021). Regression plane concept for analysing continuous cellular processes with machine learning. *Nature Communications*, *12*(1), 2532. https://doi.org/10.1038/s41467-021-22866-x

Valls, P. O., & Esposito, A. (2022). Signalling dynamics, cell decisions, and homeostatic control in health and disease. *Current Opinion in Cell Biology*, *75*, 102066.

https://doi.org/10.1016/j.ceb.2022.01.011

Wang, W., Douglas, D., Zhang, J., Kumari, S., Enuameh, M. S., Dai, Y., Wallace, C. T., Watkins, S. C., Shu, W., & Xing, J. (2020). Live-cell imaging and analysis reveal cell phenotypic transition dynamics inherently missing in snapshot data. *Science Advances*, *6*(36). https://doi.org/10.1126/sciadv.aba9319

Wang, W., Poe, D., Yang, Y., Hyatt, T., & Xing, J. (2022). Epithelial-to-mesenchymal transition proceeds through directional destabilization of multidimensional attractor. *ELife*, *11*. https://doi.org/10.7554/eLife.74866

Yang, K. D., Damodaran, K., Venkatachalapathy, S., Soylemezoglu, A. C., Shivashankar, G. V., & Uhler, C. (2020). Predicting cell lineages using autoencoders and optimal transport. *PLoS Computational Biology*, *16*(4), e1007828. https://doi.org/10.1371/journal.pcbi.1007828

Yin, H., Price, F., & Rudnicki, M. A. (2013). Satellite cells and the muscle stem cell niche. *Physiological Reviews*, *93*(1), 23–67. https://doi.org/10.1152/physrev.00043.2011

Zaritsky, A., Jamieson, A. R., Welf, E. S., Nevarez, A., Cillay, J., Eskiocak, U., Cantarel, B. L., & Danuser, G. (2021). Interpretable deep learning uncovers cellular properties in label-free live cell images that are predictive of highly metastatic melanoma. *Cell Systems*, *12*(7), 733-747.e6. https://doi.org/10.1016/j.cels.2021.05.003

Zetser, A., Gredinger, E., & Bengal, E. (1999). p38 mitogen-activated protein kinase pathway promotes skeletal muscle differentiation. Participation of the Mef2c transcription factor. *The Journal of Biological Chemistry*, *274*(8), 5193–5200. https://doi.org/10.1074/jbc.274.8.5193